Modelling of the laser surface nitriding of Ti–6Al–4V alloy—analysis of heat transfer and residual stresses

M Labudovic and **R Kovacevic***
Department of Mechanical Engineering, Southern Methodist University, Dallas, Texas, USA

Abstract: A three-dimensional finite element modelling of the laser surface nitriding of Ti–6Al–4V alloy is presented. Design capabilities of ANSYS parametric design language (APDL) were employed for this purpose. The model calculates transient temperature profiles, the dimensions of fusion zone and residual stresses in the laser surface nitrided Ti–6Al–4V alloy. Model simulations are compared with experimental results, acquired on-line using an ultra-high-speed shutter camera which is able to acquire well-contrasted images of the molten pool, and off-line using metallographical and X-ray diffraction analyses which show very good agreement. The results are further discussed to provide directions for reducing the residual stresses, as well as for feedback and process control.

Keywords: laser surface nitriding, finite element modelling, Nd:YAG laser, residual stresses, thermomechanical simulation, experiments

NOTATION

A	heat absorptivity of the laser beam on the metal surface
c	specific heat (J/kg K)
E	elastic modulus (N/mm^2)
h	heat transfer coefficient (W/m^2 K)
H	enthalphy (J/kg)
I	thermal flux density of the laser beam (J/s m^2)
k	heat conductivity (J/m s K)
$\boldsymbol{p}$	surface pressure vector (N/m^2)
P	laser beam power (J/s)
$\dot{q}$	rate of heat generation (J/s m^3)
$\dot{\boldsymbol{q}}_{ji}$	tensor of heat flow derivatives (J/mm^3 s)
Q_v	volume-specific heat flow or source density (J/mm^3 s)
$\boldsymbol{Q}$	body force vector (N/m^3)
r	distance from the centre of the laser beam (m)
r_b	effective laser beam radius (m)
S	area (m^2)
t	time (s)
Δt	incremental time (s)
T	temperature (K)
$\dot{T}$	cooling rate (K/s)
u, v, w	displacement components in the x, y and z directions respectively (m)
$\boldsymbol{u}$	displacement vector (m)
V	volume (m^3)
α	thermal expansion coefficient (K^{-1})
ε	emissivity
$\boldsymbol{\varepsilon}$	strain tensor in updated Lagrange configuration
$\dot{\varepsilon}_{ii}$	tensor of elastic volumetric strain rates (s^{-1})
$\dot{\varepsilon}_{vpij}$	tensor of viscoplastic strain rates (s^{-1})
ν	Poisson's ratio
ξ	inelastic heat fraction
ξ, ζ, χ	local coordinates
ρ	density (kg/m^3)
σ	Stefan–Boltzmann constant $= 5.670 \times 10^{-8}$ W/m^2 K^4
$\boldsymbol{\sigma}$	stress tensor in updated Lagrange configuration (N/m^2)
σ_{dij}	deviatoric stress tensor (N/mm^2)

The MS was received on 23 December 1999 and was accepted after revision for publication on 14 April 2000.
** Corresponding author: Research Center for Advanced Manufacturing, Southern Methodist University, 1500 International Parkway, Suite 100, Richardson, Dallas, TX 75081, USA.*

1 INTRODUCTION

Titanium alloys such as Ti–6Al–4V are used extensively in the aerospace industry, where their excellent corrosion resistance and high strength–weight ratio are of prime consideration. However, they suffer from poor surface wear resistance which limits further applications in tribological systems [1]. A number of surface modification techniques have been used to improve the wear properties of titanium alloys by modifying either surface composition or microstructure.

Conventional nitriding techniques, such as ion nitriding, gaseous nitriding, salt bath nitriding and others, utilize the formation of TiN in the surface layer as a result of nitrogen diffusion [2]. The thickness of the layer is a function of the process temperature, time and nitrogen partial pressure. However, these processes have the disadvantage of requiring high temperatures and extensive processing times.

Ion implantation has emerged as a new technique to improve surface hardness of titanium alloys [3]. When ion species such as nitrogen, carbon and boron are implanted into the surface layer of titanium alloys, they form hard titanium-base metallic compounds such as TiN, TiC and TiB, giving a hardened surface layer of only a few nanometres.

The wear resistance of titanium can also be improved through chemical or physical vapour-phase coating processes, but research has shown that the success of the hard surface coat is influenced by the substrate roughness, which in turn affects the adhesive strength of the coating on the titanium substrate [4]. Furthermore, the poor load-bearing capacity of the titanium alloy results in plastic deformation of the substrate, caused by high contact stresses, which result in coat failure and peeling [5].

Laser processing techniques involving laser surface melting, nitriding or alloying are widely used for surface modification [6]. In particular, laser surface nitriding is accomplished by melting the surface of the titanium alloy using a focused laser beam in a nitrogen gas environment to form a hard titanium nitride layer. As the process involves surface melting, titanium nitride formation and rapid solidification, the composition, structure, hardness and surface roughness of the treated surface are changed. The shrinkage effect in the melt zone may also produce surface residual stresses, which affect the fatigue and fretting fatigue resistance.

It is established that laser surface treatments generally result in predominantly tensile residual stresses within the processed layer [7]. In some cases, the severity of the stresses may be such that surface layer microcracking occurs. Indeed, such crack formation has frequently been observed to be specifically problematic in the case of laser-nitrided titanium alloys [8], although crack-free layers were reported to be possible when the volume fraction of the hard phase TiN was kept low and the hard layer thickness was reduced [9]. Morten *et al.* [10] reported that surface cracking could also be eliminated by preheating the substrate before laser melting. The preheating treatment has the effect of reducing the steep temperature gradients that are generated during laser processing, thereby reducing the creation of any thermal stresses. It has also been shown that the tendency for cracking in single laser tracks may be reduced by the dilution of the alloy gas with an inert carrier gas or by a combination of alloy gas dilution and preheating [10]. However, applications where controlled preheating may be employed are limited. It is, therefore, important to understand the details of residual stress development associated with laser surface treatments with and without preheating. Furthermore, the production of a laser-treated surface relies on the successive overlapping of adjacent laser tracks [8]. Single-track studies have most recently been used to define process parameter regimes where microcracking does not occur [11]. However, in spite of the possibility of producing crack-free single tracks, the effect of overlapping adjacent tracks on the residual stress distribution should be accurately understood if the technique is to find viable application in the treatment of engineering components.

Another equally important issue arises from the recent trend towards automation. Various deviations from ideal conditions during laser surface treatments have been found to display distinct characteristic signatures on the surface temperature patterns [12]. A capability of computationally predicting these effects allows the possibility of constructing a weld quality monitoring or controlling system. Therefore, the recent interest in modelling of laser surface treatment processes is motivated by two related requirements:

1. In order to maintain consistent surface quality, it is essential to correlate the mechanical properties of the final structure to the laser processing parameters, such as energy input, travel speed of the laser beam and preheat temperature. Collectively, these parameters dictate the thermal histories at each location of the treated surface. In turn, these temperature variations in terms of local cooling rates to a large extent determine the final microstructure, residual stresses and mechanical properties.
2. As indicated by Giedt [13], a simpler simulation that accommodates the molten pool convection only empirically may be adequate for many automation applications requiring real-time process monitoring and control. Automated systems are currently being investigated for laser processing of several materials. The vision system is used in laser processing for process monitoring and for detecting any deviations from ideal conditions owing to various anomalies. Real-time process correction may be provided by comparing the measured signal with that predicted by a model.

The laser beam can be considered as a moving heat source with a certain power density distribution that imposes a boundary condition on the substrate surface. The classical approach to modelling the heat flow induced by a distributed heat source moving over the surface of a semi-infinite solid starts with the solution of the heat diffusion equation to determine a point source [14]. Following the classical analysis of temperature variations resulting from moving heat sources by Rosenthal [15], a number of studies have added realistic

effects, such as temperature-dependent material properties and radiative and convective boundary conditions, on the workpiece surface. Furthermore, instead of the idealized point and line source variations, closer approximations to the heat inputs, including Gaussian and more complex profiles, have been examined. Many of these efforts have been summarized by Goldak *et al.* [16].

This paper presents a new three-dimensional model of the laser surface nitriding of Ti–6Al–4V alloy utilizing the efficient solution procedures of the finite element capabilities of ANSYS parametric design language (APDL). The results of the model are compared with experimental results. A high-power Nd:YAG laser of 1.06 μm wavelength operating in continuous wave (CW) mode was used to generate single as well as overlapped laser tracks on Ti–6Al–4V alloy. An ultra-high-speed shutter camera with pulsed laser illumination has been used as the process detector, producing well-contrasted images of the molten pool. The physical dimensions of the fusion zone (FZ) were measured and compared with the predictions of the model. Since the geometrical features of the molten pool can be used as an efficient feedback to estimate the molten depth, a model is built to explore the correlation between molten depth, molten pool geometry and processing parameters (laser power and travel speed). Finally, residual stresses predicted by the model were compared with those obtained experimentally by X-ray analysis of the nitrided surfaces. The issues related to the reduction of residual stresses are addressed.

2 EXPERIMENT

The experimental set-up which consists of an Nd:YAG laser, a two-axis computer numerically controlled (CNC) positioning system, a laser strobe vision system, shielding gas and the workpiece is shown in Fig. 1. Fibre optics conduct a laser light of 337 nm wavelength to illuminate the Nd:YAG laser treatment area. The illuminating laser is a nitrogen pulse laser of 5 ns pulse duration, synchronizing with the high-speed shutter of the camera. The camera of the laser strobe vision system is equipped with a UV filter that only allows light near a 337 nm wavelength to pass. During the illumination period, the intensity of the illuminating laser can suppress the spatter and plasma light. In addition, owing to the reflection of the mirror-like molten pool, a well-contrasted image of the molten pool can be obtained. Nitrogen is used as an alloying gas and as a shielding gas.

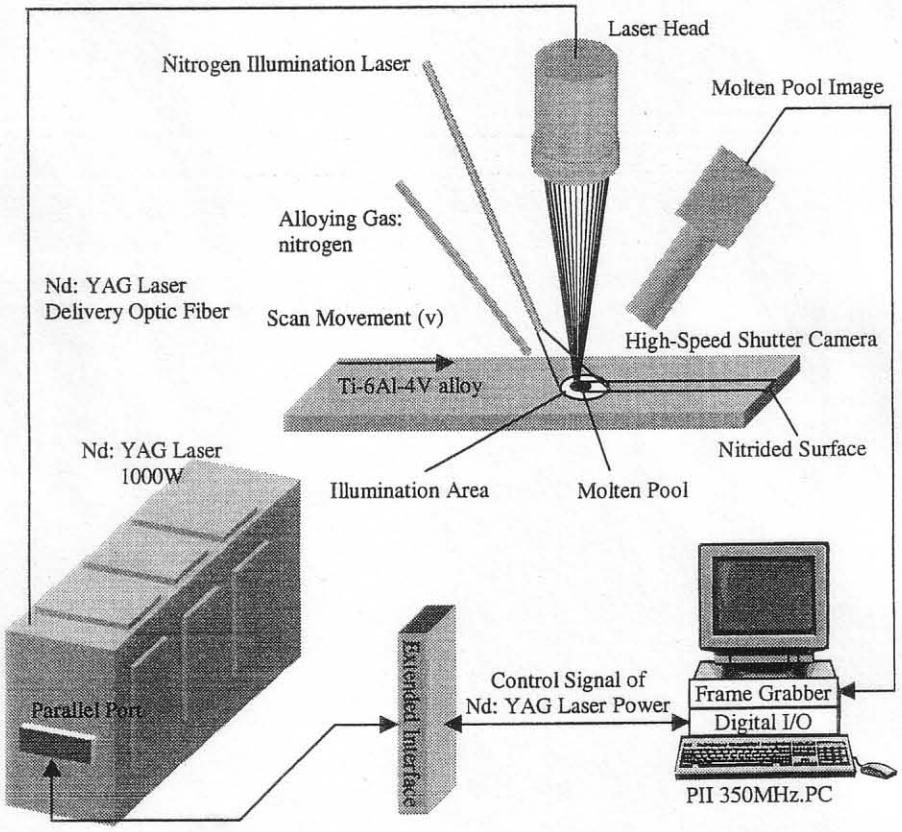

Fig. 1 Experimental set-up

A frame grabber installed on a PII 350 PC computer acquires images from the ultra-high shutter speed camera at 30 Hz. Image processing and recognition is completed on the same computer.

3 PHYSICAL DESCRIPTION OF THE MODEL

The following assumptions were made in the formulation of the finite element model:

1. The laser beam is incident at an angle θ to the surface of the workpiece in order to prevent back-reflections from the workpiece.
2. The workpiece is initially at 298 K. Both the workpiece and the coordinate mesh are fixed and the laser beam moves in the positive z direction with a constant velocity, v.
3. All thermophysical as well as mechanical properties are considered to be temperature dependent. These properties are shown in Table 1 and Fig. 2 [**17**, **18**]. The temperature-dependent stress–strain curves used in the model are shown in Fig. 3 [**19**].
4. The laser beam diameter is defined as the diameter in which the power density is reduced from the peak value by a factor of e^2 [**20**].
5. During the simulation, the thermal load is given in the form of the thermal flux density, which obeys normal distribution as follows [**21**]:

$$I = \frac{2AP}{\pi r_b^2} \exp\left(-\frac{2r^2}{r_b^2}\right) \tag{1}$$

The mean thermal flux density within the area of laser beam scanning on the titanium alloy surface is [**21**]

$$I_m = \frac{1}{\pi r_b^2} \int_0^{r_b} I(2\pi r)\, dr$$

$$= \frac{2\pi}{\pi r_b^2} \int_0^{r_b} \frac{2AP}{\pi r_b^2} \exp\left(-\frac{2r^2}{r_b^2}\right) r\, dr$$

$$= \frac{0.865AP}{\pi r_b^2} \tag{2}$$

6. The latent heat of fusion is simulated by an artificial increase in the liquid specific heat according to Brown and Song [**22**] and the relationship between the enthalpy, H, density, ρ, and specific heat, c:

$$H = \int \rho c(T)\, dT \tag{3}$$

7. Since laser surface modification involves very rapid melting and solidification, convective redistribution of heat within the molten pool is not significant (whereas it is in other processes where a liquid pool is permanent). Convective flow of heat, therefore, is neglected.
8. Since the laser is defocused, there is no keyhole

Table 1 Emissivity and Poisson's ratio of titanium alloy Ti–6Al–4V used in the finite element model [**17**]

Temperature (K)	300	400	500	600	700	800	900	1000	1100	1200	1300	1400	1500	1600
Emissivity	0.12	0.15	0.17	0.20	0.22	0.25	0.55	0.59	0.60	0.60	0.60	0.60	0.60	0.60
Poisson's ratio	0.33	0.33	0.30	0.33	0.33	0.33	0.33	0.33	0.33	0.33	0.33	0.33	0.33	0.33

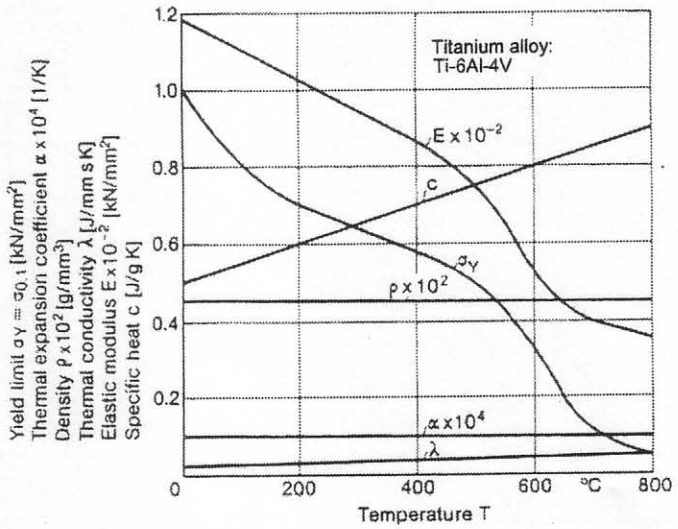

Fig. 2 Thermal and mechanical characteristics of titanium alloy Ti–6Al–4V as a function of temperature [**18**]

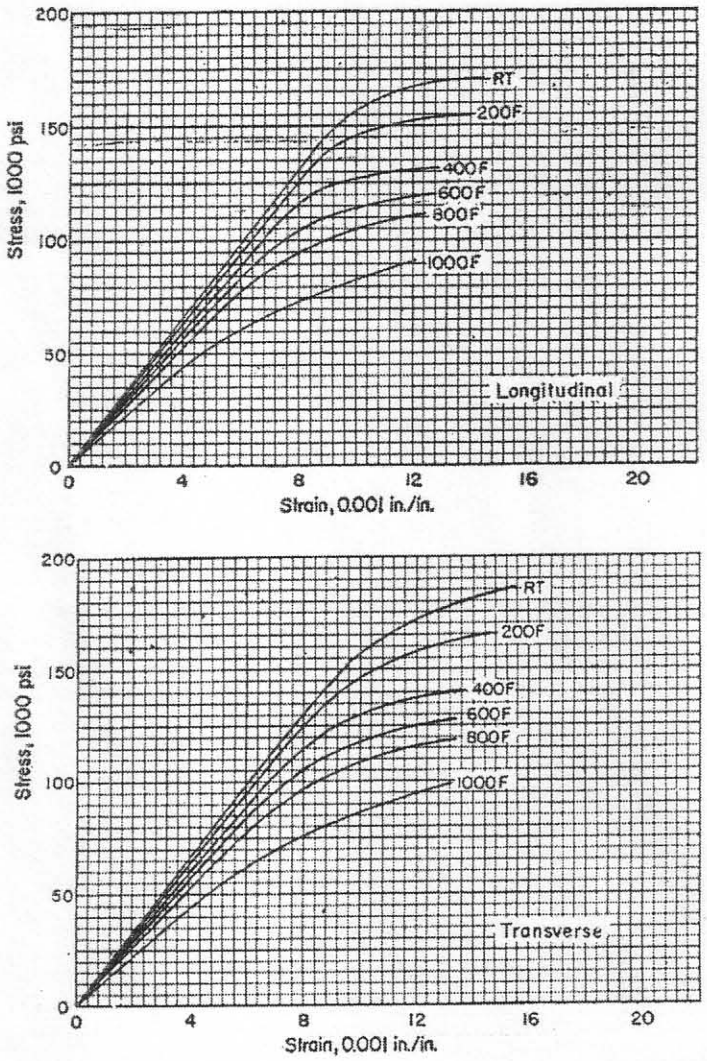

Fig. 3 Stress–strain curves for titanium alloy Ti–6Al–4V at different temperatures [19]

formation and the energy absorption of the plasma can be neglected.

4 MATHEMATICAL DESCRIPTION OF THE MODEL

For analysis of the movement and deformation of the configuration in the finite element method (FEM), suppose that the equilibrium states at all time steps from time 0 to t have been obtained. Then, according to the virtual work principle [23], the equilibrium equation at time $t + \Delta t$ can be expressed as follows:

$$\int_V \boldsymbol{\sigma} \cdot \delta\boldsymbol{\varepsilon}\, \mathrm{d}V = \int_V \boldsymbol{q} \cdot \delta\boldsymbol{u}\, \mathrm{d}V + \int_S \boldsymbol{p} \cdot \delta\boldsymbol{u}\, \mathrm{d}S \tag{4}$$

To account for the large deformation, the following shape functions, with extra shape functions (ESFs) for elements of eight-node bricks, are used:

$$\begin{aligned}
u = {} & \tfrac{1}{8}[u_{\mathrm{I}}(1-\xi)(1-\zeta)(1-\chi) \\
& + u_{\mathrm{J}}(1+\xi)(1-\zeta)(1-\chi) \\
& + u_{\mathrm{K}}(1+\xi)(1+\zeta)(1-\chi) \\
& + u_{\mathrm{L}}(1-\xi)(1+\zeta)(1-\chi) \\
& + u_{\mathrm{M}}(1-\xi)(1-\zeta)(1+\chi) \\
& + u_{\mathrm{N}}(1+\xi)(1-\zeta)(1+\chi) \\
& + u_{\mathrm{O}}(1+\xi)(1+\zeta)(1+\chi) \\
& + u_{\mathrm{P}}(1-\xi)(1+\zeta)(1+\chi)] \\
& + u_1(1-\xi^2) + u_2(1-\zeta^2) + u_3(1-\chi^2) \\
v = {} & \tfrac{1}{8}[v_{\mathrm{I}}(1-\xi)\cdots] \qquad \text{(analogous to } u\text{)} \\
w = {} & \tfrac{1}{8}[w_{\mathrm{I}}(1-\xi)\cdots] \qquad \text{(analogous to } u\text{)}
\end{aligned} \tag{5}$$

where u_I (I = I, J, K, L, M, N, O, P) are nodal displacements.

Discretization of this problem is accomplished by means of the standard finite element procedure. The result of aggregation is a group of non-linear equations. The Newton–Raphson method is used to linearize these equations:

$$[\mathbf{K}]\{\Delta \boldsymbol{u}\} = \{F^{\mathrm{a}}\} - \{F^{\mathrm{nr}}\} \tag{6}$$

where

$[\mathbf{K}] = \int_V [\mathbf{B}]^{\mathrm{T}}[\mathbf{D}^{\mathrm{ep}}][\mathbf{B}]\,\mathrm{d}V$ is the tangential stiffness matrix
$[\mathbf{B}]$ = strain–displacement matrix
$[\mathbf{D}^{\mathrm{ep}}]$ = elastoplastic stress–strain matrix
$\{\Delta \boldsymbol{u}\}$ = displacement increment at the element nodes
$\{F^{\mathrm{a}}\}$ = applied force vector
$\{F^{\mathrm{nr}}\} = \int_V [\mathbf{B}]^{\mathrm{T}}\{\boldsymbol{\sigma}\}\,\mathrm{d}V$ is the Newton–Raphson restored force vector

For the thermomechanical coupled system, the thermal equilibrium equation for analysis of heat transfer in a domain D can be written as

$$k\left(\frac{\partial^2 T}{\partial x^2} + \frac{\partial^2 T}{\partial y^2} + \frac{\partial^2 T}{\partial z^2}\right) + \dot{q} = \rho c \dot{T} + v\frac{\partial T}{\partial z} \tag{7}$$

To obtain the solution from the thermal equilibrium equation, boundary conditions and initial conditions are needed.

The initial condition is

$$T(x, y, z, 0) = T_0, \qquad \text{for } (x, y, z) \in D \tag{8}$$

The essential boundary condition is:

$$T(x, 0, z) = T_0 \tag{9}$$

on the boundary S_1 for $(x, z) \in S_1$ and $t > 0$. Here, S_1 represents the bottom surface of the plate.

The natural boundary conditions can be defined by

$$k_n \frac{\partial T}{\partial n} - q + h(T - T_0) + \sigma\varepsilon(T^4 - T_0^4) = 0 \tag{10}$$

on the boundary S_2 for $(x, y, z) \in S_2$ and $t > 0$. Here S_2 represents those surfaces that are subjected to radiation, convection and imposed heat fluxes.

The inclusion of temperature-dependent thermophysical and mechanical properties and a radiation term in the above boundary condition makes this type of analysis highly non-linear. Since the incorporation of radiation effects is found to increase the solution time by as much as a factor of 3, an empirical relationship as proposed by Vinokurov [**24**] was used:

$$H = 2.4 \times 10^{-3}\varepsilon T^{1.61} \tag{11}$$

Equation (10) combines the effect of radiation and convection into a 'lumped' heat transfer coefficient. The associated loss in accuracy using this relationship is estimated to be less than 5 per cent [**24**].

The fundamental equation of thermomechanics of elastic–viscoplastic continua follows from the constitutive model [**18**]:

$$c_\rho \dot{T} + \dot{q}_{ii} = \dot{Q}_{\mathrm{v}} - \frac{E_\alpha T}{1 - 2\nu}\,\dot{\varepsilon}_{ii} + \xi\sigma_{\mathrm{d}ij}\,\dot{\varepsilon}_{\mathrm{vp}ij} \tag{12}$$

where ξ is the inelastic heat fraction; $\xi \leqslant 1.0$ allows for the fact that some inelastic deformation energy is dissipated in heat but may appear in a microstructural change.

The restriction to plastic behaviour without viscosity is adequate for the majority of laser surface treatment residual stress problems [**18**]. Therefore, the viscosity behaviour in equation (11) is neglected.

5 NUMERICAL DESCRIPTION OF THE MODEL AND COMPUTER ALGORITHM

ANSYS provides a convenient means of numerically modelling laser surface modification processes. This requires an integration of the heat conduction equation with respect to time. In the finite element formulation, this equation can be written for each element as

$$[\mathbf{C}_T]\{\dot{\boldsymbol{T}}\} + [\mathbf{K}_T]\{\boldsymbol{T}\} = \{\boldsymbol{Q}\} \tag{13}$$

where

$[\mathbf{C}_T] = \int_V \rho c[\mathbf{N}][\mathbf{N}]^{\mathrm{T}}\,\mathrm{d}V$ = heat capacity matrix
$[\mathbf{N}]$ = shape function matrix
$[\mathbf{K}_T] = \int_V k[\mathbf{B}][\mathbf{B}]^{\mathrm{T}}\,\mathrm{d}V$ = heat conduction matrix
$\{\boldsymbol{T}\}$ and $\{\dot{\boldsymbol{T}}\}$ = nodal temperature vector and nodal temperature rate vector respectively
$\{\boldsymbol{Q}\}$ = heat flux vector

The moving laser beam is simulated using ANSYS parametric design language (APDL) to provide the heat boundary conditions at different positions at different times. The first iteration in the solution procedure solves the system equations at an assumed starting temperature (298 K), and subsequent iterations use temperatures from previous iterations to calculate the thermal conductivity and specific heat matrices. The iterative process continues for time period T until a converged solution is achieved or until the dynamic equilibrium of heat exchange is established. Based on the image analysis of the molten pool performed in reference [**25**], it is concluded that the geometric shape of the molten pool will be in steady state after 2 s. Therefore, $T = 2$ s is used as the time period T when dynamic equilibrium of heat exchange is established.

A study of the heat transfer problem will allow the determination of the temperature distribution within a

body. It will then be possible to determine the amount of heat moving into or out of the body, and the residual stresses. The basic equation for thermomechanical coupled calculation is as follows:

$$\begin{bmatrix} [0] & [0] \\ [0] & [C] \end{bmatrix} \begin{Bmatrix} \{\dot{u}\} \\ \{\dot{T}\} \end{Bmatrix} + \begin{bmatrix} [K] & [0] \\ [0] & [K_T] \end{bmatrix} \begin{Bmatrix} \{u\} \\ \{T\} \end{Bmatrix} = \begin{Bmatrix} \{F\} \\ \{Q\} \end{Bmatrix} \quad (14)$$

where $\{F\}$ is the force vector including the applied nodal force and the force caused by thermal strain.

The residual stresses caused by inhomogeneous thermal expansion (or contraction) are termed 'thermal stresses'. Elastic thermal stresses disappear after removal of the inhomogeneous temperatures that have caused them. For this reason, many authors do not classify them as residual stresses. Where major differences in temperature exist, the thermal stresses give rise to plastic deformations. After removal of the temperature differences, residual stresses remain. The plastic behaviour is incorporated in the model by making use of the experimental data given in Fig. 3.

A point worth stressing is the need to incorporate microstructural transformations into the analysis, which depends not only on the chemical composition of the material but also on its thermal history. These residual stresses caused by microstructural transformation are termed 'transformation stresses'. The decoupling and mutual influence of the temperature field, stress and deformation field and microstructural state field are shown in Fig. 4 [**18**]. The diagram of Fig. 4 has been extended in Fig. 5 to emphasize the influence of transformation behaviour and to indicate the essential input and output parameters referring to finite element analysis. ANSYS provides the performance of an indirect coupled-field analysis implementing the above equations for calculating residual stresses. In this method, two sequential analyses are carried out using results from the first analysis as loads for the second analysis. The algorithm for a residual stress analysis is summarized in Fig. 6.

6 MODELLING RESULTS

6.1 Analysis of heat transfer

Comparison of experimental and simulated results may allow the estimation of the relative importance and role of the complex physical interactions that govern laser surface modification processes. Experiment and simulation were compared on a Ti–6Al–4V alloy specimen with dimensions $20 \times 10 \times 50$ mm. The finite element mesh is shown in Fig. 7. Because of symmetry about the z–y plane, only half the plate is considered. The model was run for both the duration of the laser heating and for the subsequent cooling period using different powers (in the range 300–1200 W) and scanning speeds (in the range 5–15 mm/s). Figure 8 shows typical analysis results from the use of 10 mm/s scanning speed and 800 W laser power in a 100% N_2 shielding atmosphere.

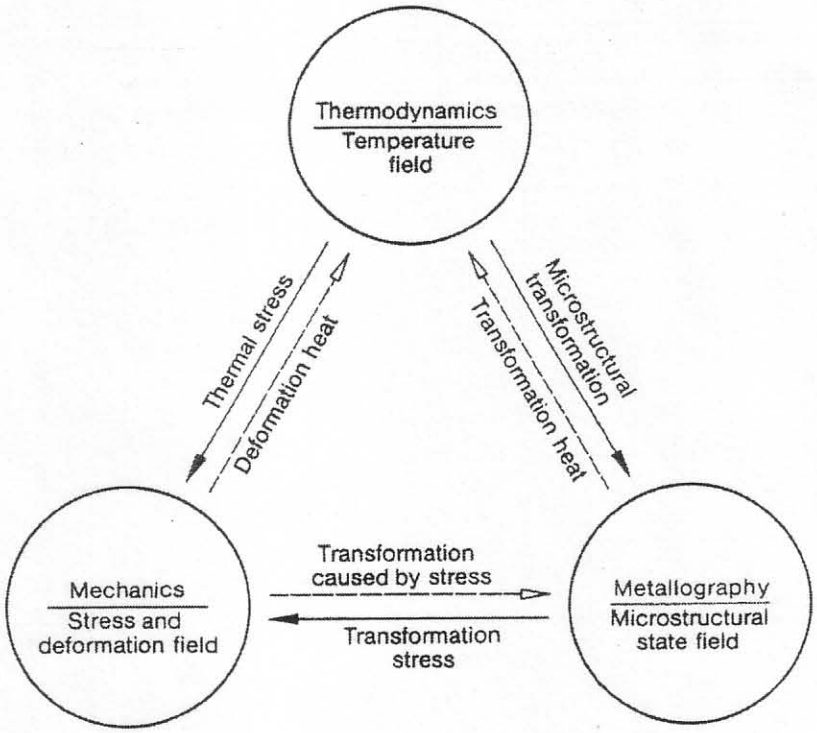

Fig. 4 Decoupling and mutual influence of the temperature field, the stress and deformation field and the microstructural state field [**18**]

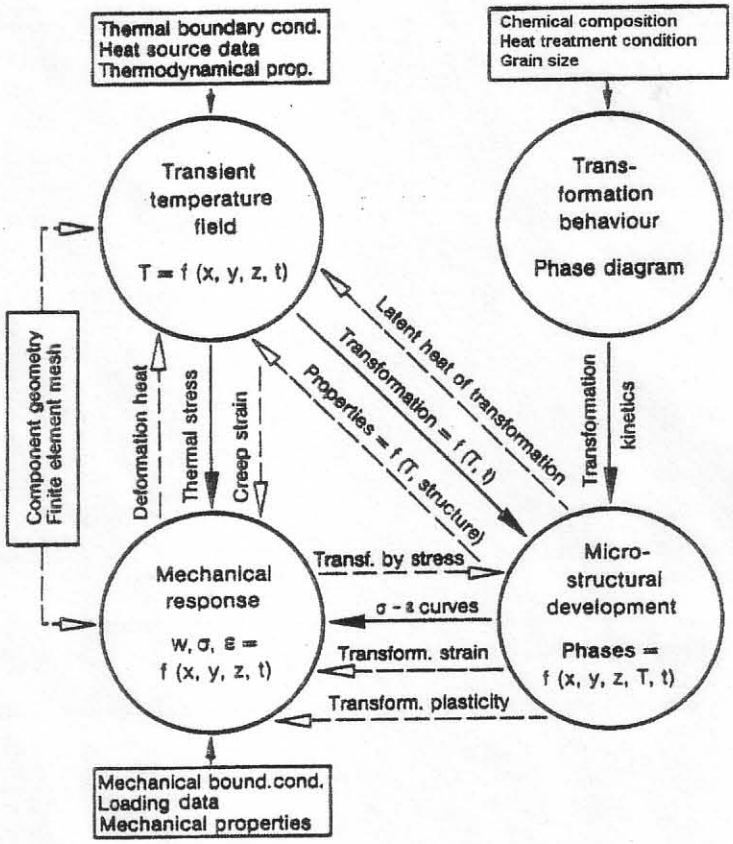

Fig. 5 Extended diagram of Fig. 4, emphasizing the influence of microstructural transformation

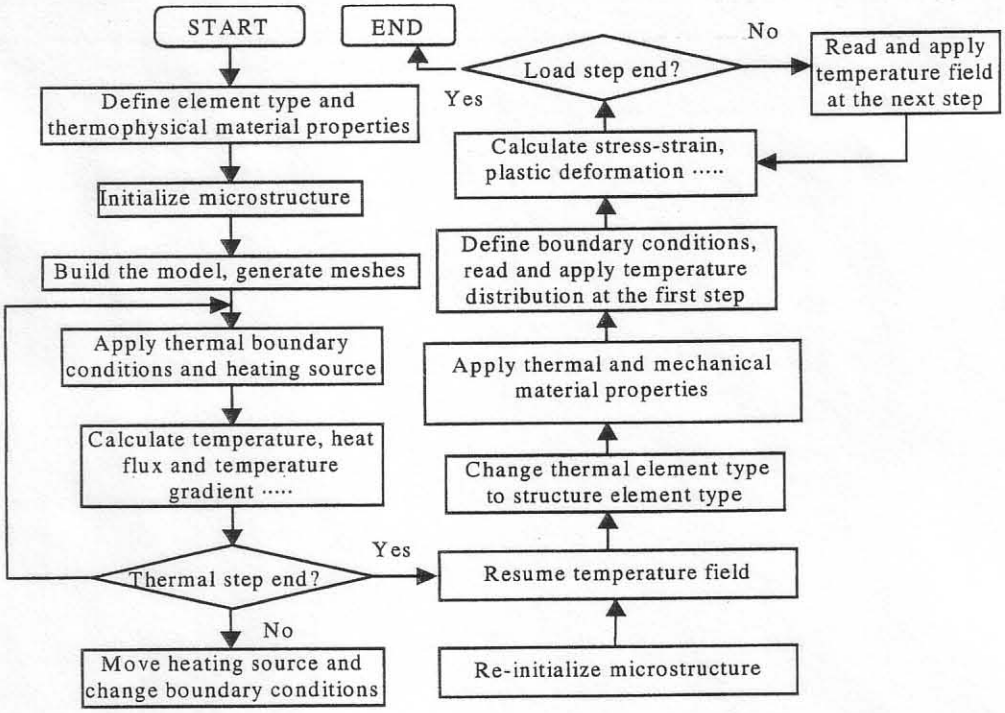

Fig. 6 Computer algorithm

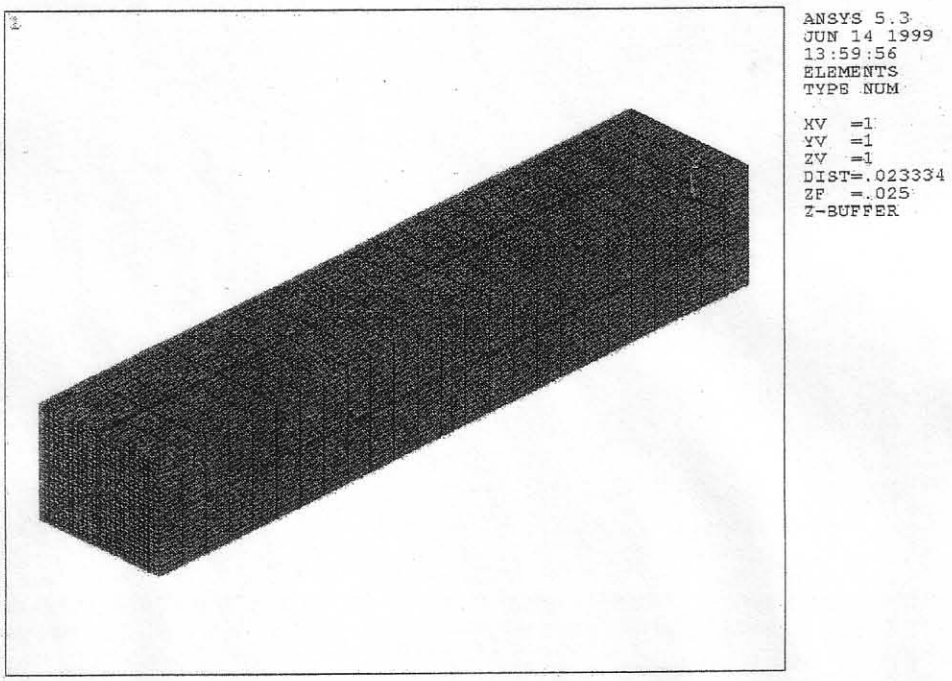

Fig. 7 Finite element mesh for ANSYS analysis

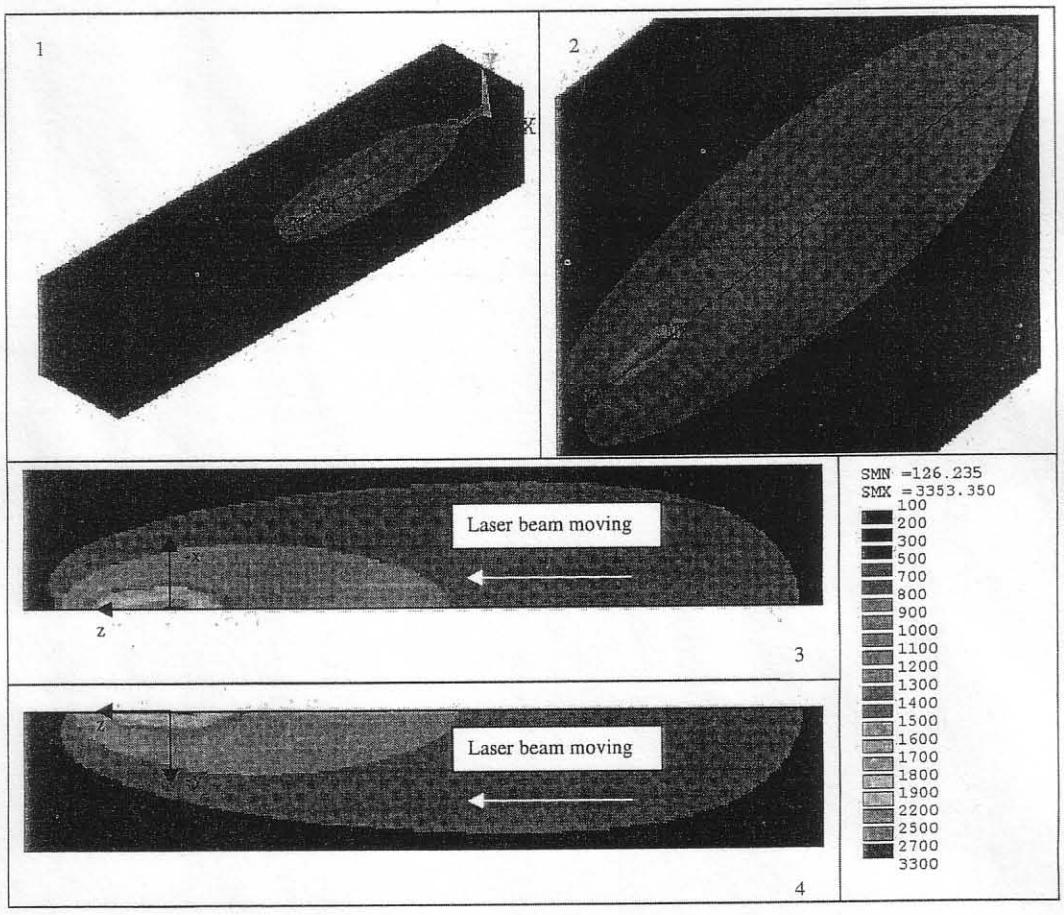

Fig. 8 Temperature distribution during laser gas nitriding of titanium alloy Ti–6Al–4V (laser power 800 W, scanning speed 10 mm/s, shielding atmosphere 100% N_2): (1) overview; (2) zoom view; (3) top view; (4) right-hand view

The data generated during the solution procedure include the depth of the 1630 °C (1900 K) isotherms which approximately represent the FZ boundary. These data are then used for comparison with experimental results. Figure 9 shows micrographs of the cross-sections of laser-nitrided surfaces obtained for different laser processing parameters (laser power and scanning speed) and for a 100% N_2 shielding atmosphere. From such micrographs, the depth and width of the FZ may be measured. Just as this laser-modified surface was physically sectioned, a section through the centre-line of the model can be taken. ANSYS model predictions of the FZ are superimposed on these micrographs. These isotherms represent the positions that have been heated to a maximum temperature of 1630 °C.

The model was also run for different compositions of the shielding atmosphere. The temperature of each nodal point within the solid was calculated as a function of time. For each laser power and scanning speed, the maximum depth and diameter of the 1630 °C temperature contours were measured. These measurements have been plotted in Fig. 10 and may be compared directly with the experimental measurements of the FZ dimensions.

The calculated peak surface temperature can be used together with the phase diagram data (Fig. 11) to correlate with the as-solidified microstructures. For example, for titanium alloy nitrided in 50 vol % N_2, the calculated peak temperature of 2180 °C (2453 K) corresponds to the solubility of ~ 7% N in liquid Ti. Solidification of liquid for $N \leqslant 7$ at % under rapid

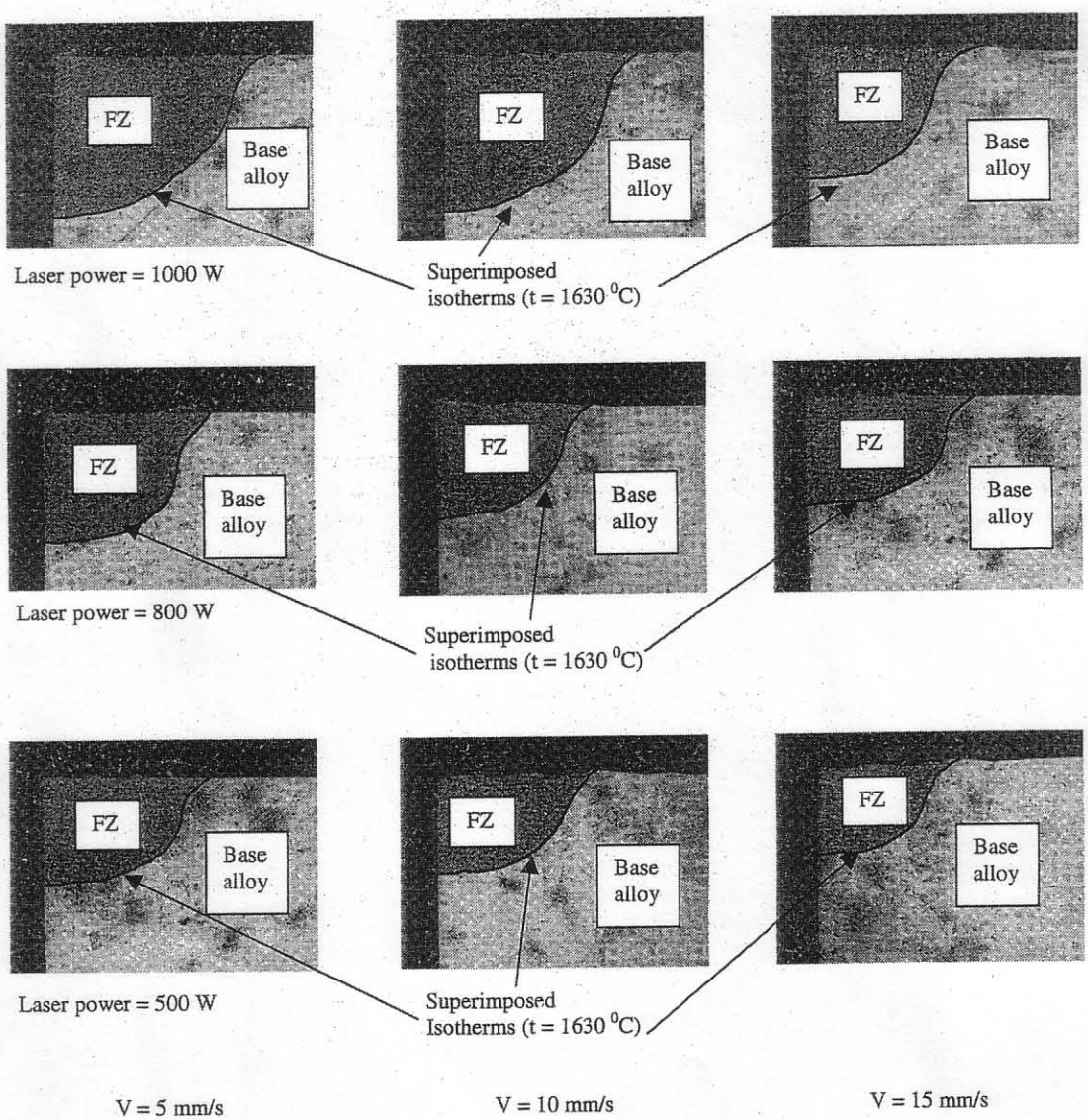

Fig. 9 Micrographs of the cross-sections of titanium alloy Ti–6Al–4V surface treated in a pure N_2 (100 vol %) gas shield and for different laser powers and scanning speeds, showing model predictions of the FZ boundaries

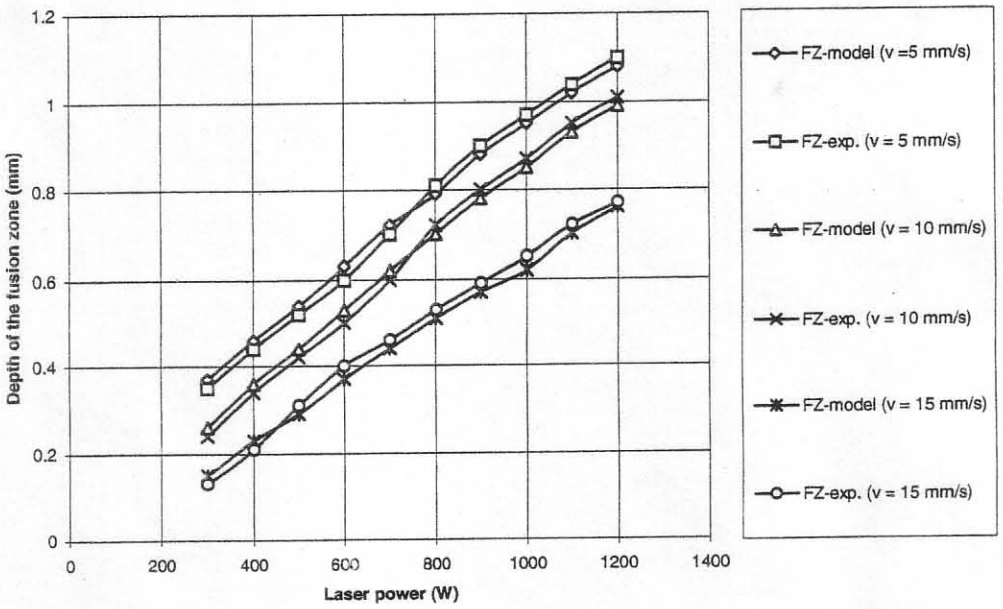

(a)

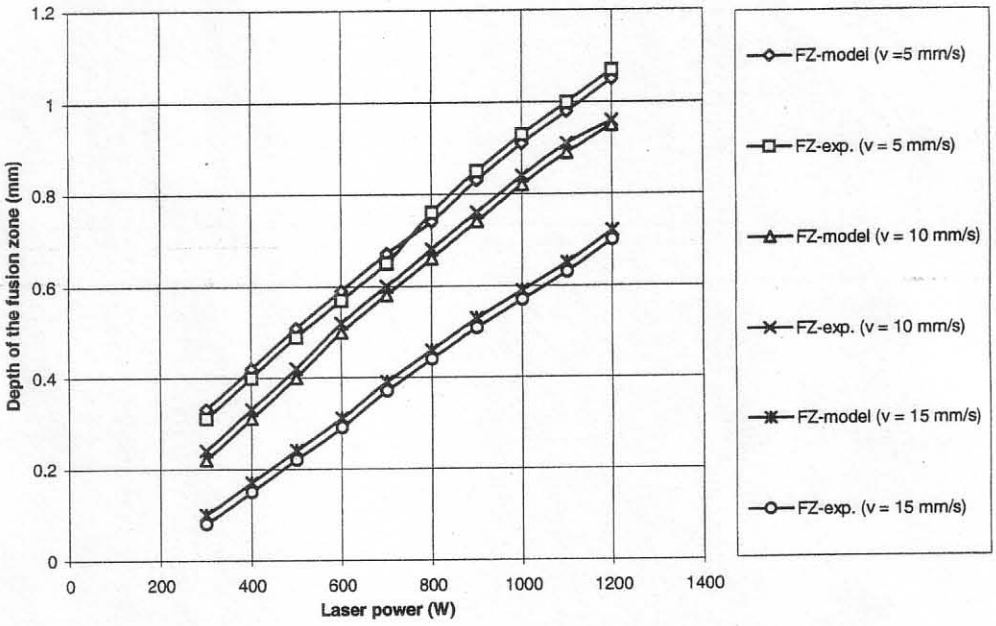

(b)

Fig. 10 Fusion zone depths compared with model predictions for different shielding atmosphere compositions, laser powers and scanning speeds: (a) 50% N_2/50% Ar; (b) 100% Ar

cooling conditions is expected to follow the sequence: $L \rightarrow \alpha$; $L + \alpha \rightarrow \beta$; with β transforming to martensitic α' in the solid state. This sequence is consistent with the observed microstructure (Fig. 12) showing an α layer from the peritectic reaction ($L + \alpha \rightarrow \beta$) that produced the α' microstructure. This is confirmed by X-ray analysis, as shown in Fig. 13. Similarly, at the peak temperature of 3080 °C (3353 K) for the titanium alloy treated in 100% N_2, the solubility level of nitrogen in liquid Ti is ~30% N. A possible rapid cooling

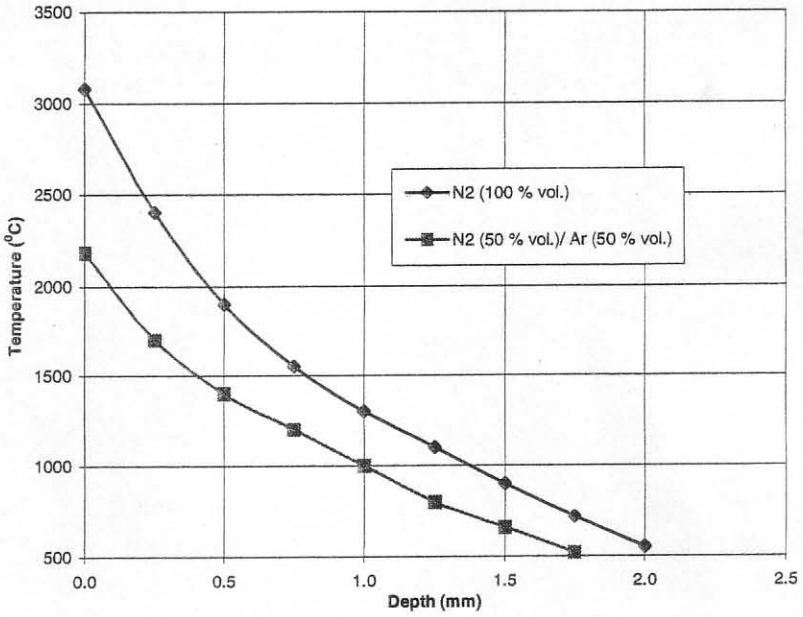

(a)

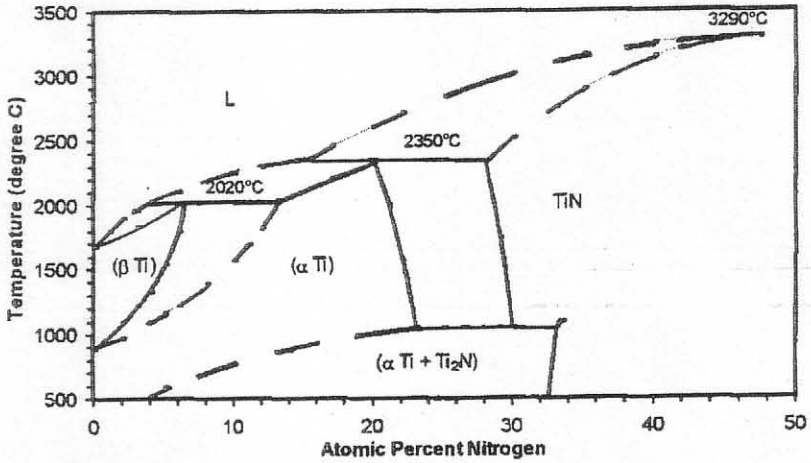

(b)

Fig. 11 (a) Calculated maximum temperature in titanium alloy Ti–6Al–4V laser treated in Ar–N_2 mixtures with different N_2 contents; (b) Ti–N phase diagram for comparison [1]

sequence for $N \leqslant 30$ at % is: $L \rightarrow TiN$; $L \rightarrow \alpha$; $L + \alpha \rightarrow \beta$; $L \rightarrow \beta$; with β transforming to α'. This sequence is consistent again with the observed microstructures (Fig. 14) and X-ray analysis (Fig. 15) showing the presence of TiN, α and α'.

The isotherms corresponding to 1630 °C are superimposed on the images of the molten pool acquired on-line by a laser strobe vision system (Fig. 16), showing very good agreement between the simulated results and the results obtained by the image processing algorithm developed in reference [25] for validation. Furthermore, the results are validated for other processing parameters as well (scanning speed, laser power) (Fig. 17). The size and shape of the molten region obtained on-line is almost the same as those obtained by simulation for all applied laser powers and scanning speeds. In addition, by observing the molten pool it can be seen that the pool is deeper at the end than on the front because of the heat accumulation. However, an increase in the laser power and decrease in the scanning speed result in

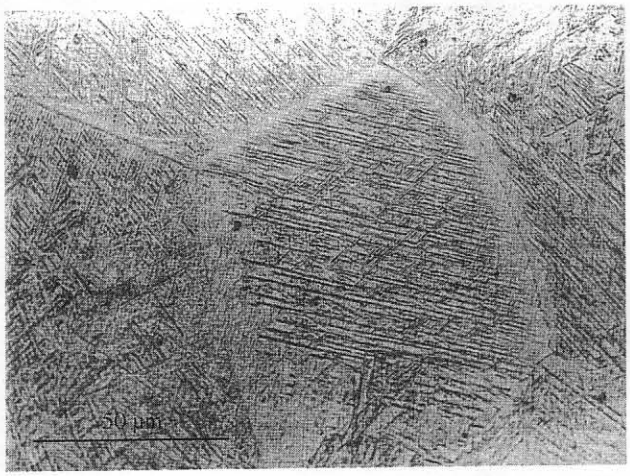

Fig. 12 Micrograph showing titanium alloy Ti–6Al–4V surface treated under a mixture of Ar (50 vol %) and N_2 (50 vol %)

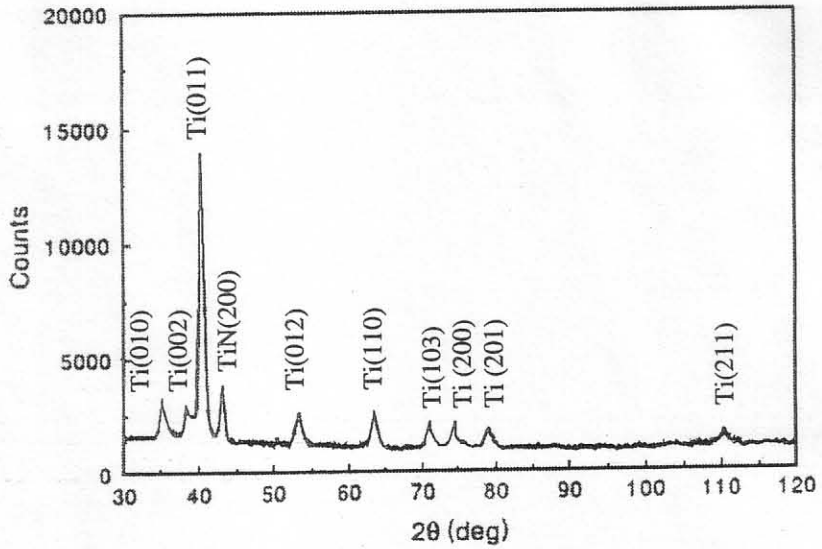

Fig. 13 X-ray diffraction spectrum taken from the titanium alloy Ti–6Al–4V surface treated under a mixture of Ar (50 vol %) and N_2 (50 vol %)

a wider molten pool. The display of these distinct characteristic signatures on the surface temperature patterns makes it possible to estimate the depth of the molten pool, which is the major issue of the recent trend towards surface modification automation. Therefore, since there are no reliable sensors presently available for the remote real-time measurement of the absolute molten pool temperature, the obtained results can be used for molten pool depth estimation and close-loop control of laser surface modification. The real-time control of the process, in order to produce a more stable and repeatable molten pool depth, and adaptation of the model to a more complex shape of the processed parts will be challenging objectives in subsequent research.

6.2 Analysis of residual stresses

The distribution of residual stresses, obtained by finite element modelling, resulting from the use of 10 mm/s scanning speed and 800 W laser power in a 100% N_2 shielding atmosphere is shown in Figs 18 to 20. Surface residual stresses were also investigated using the X-ray diffraction technique. X-ray residual stress calculations were undertaken perpendicular to the direction of the laser track using the $\sin^2 \psi$ method [**26**]. The technique is not described here in detail as the theoretical background and basic principles have been recently summarized [7]. The distribution of residual stresses within a single melt track obtained by finite element modelling is compared with that obtained by the X-ray diffraction

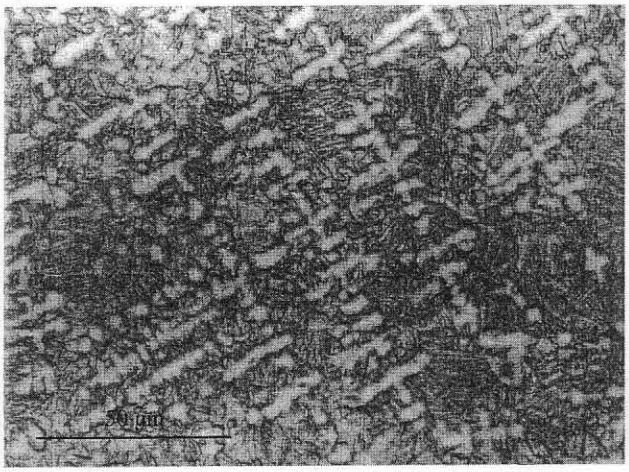

Fig. 14 Micrograph showing titanium alloy Ti–6Al–4V surface treated under a pure N_2 (100 vol %) gas shield

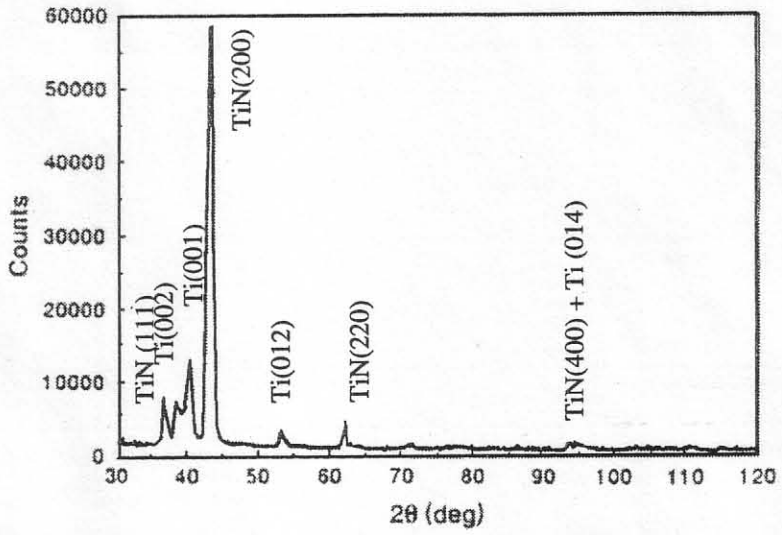

Fig. 15 X-ray diffraction spectrum taken from the titanium alloy Ti–6Al–4V surface treated under a pure N_2 (100 vol %) gas shield

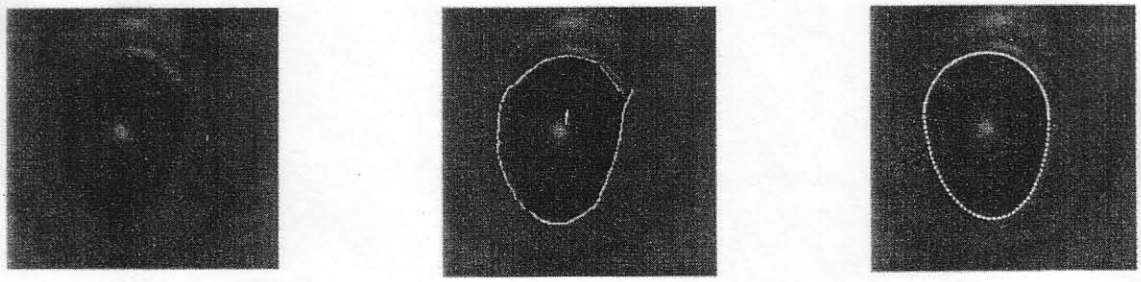

Fig. 16 Comparison of the FZ boundaries obtained by the processing results of the edge detector with those obtained by the model: (a) original image acquired by high-speed shutter camera; (b) processing result of edge detector; (c) modelling result

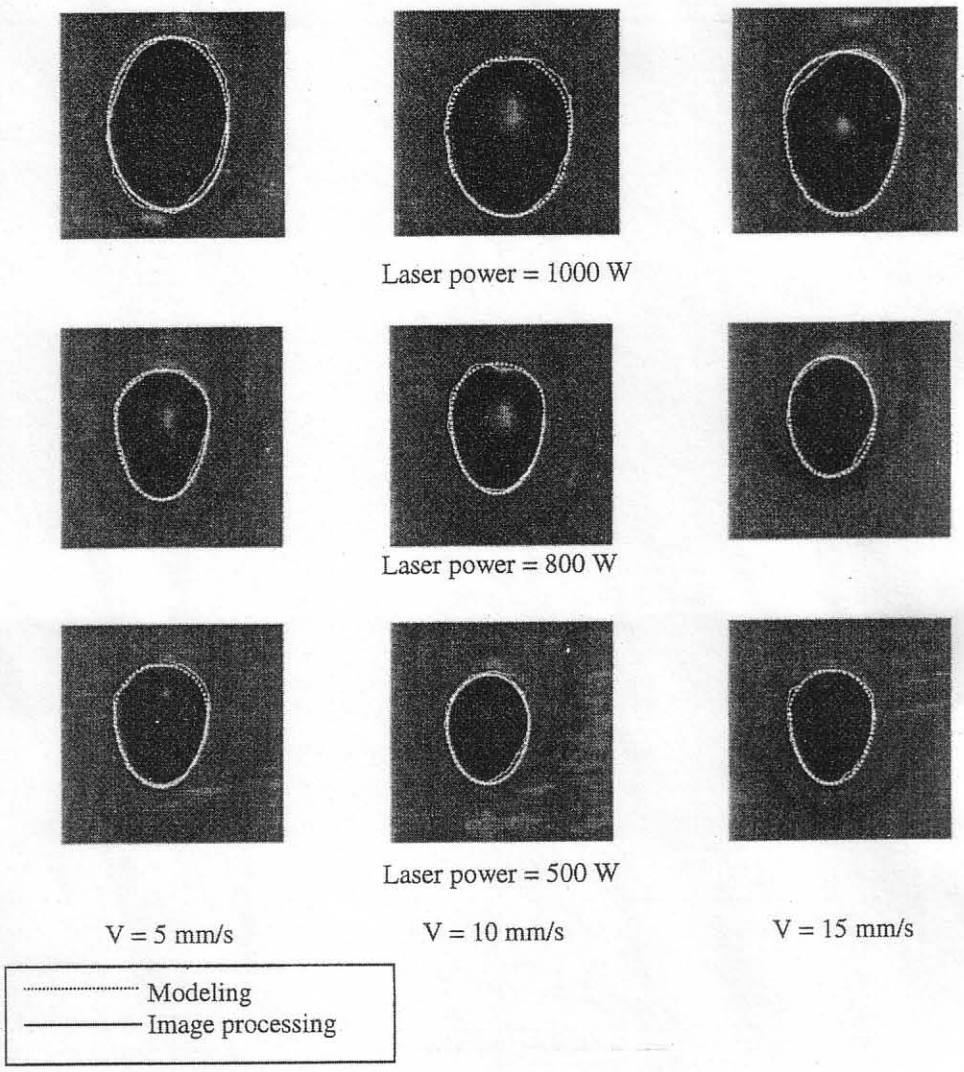

Fig. 17 Comparison of the FZ boundaries acquired on-line by a high-speed shutter camera with those obtained by the model, for different scanning speeds and laser powers

technique, showing satisfactory agreement (Fig. 21). The figure indicates that, within the shallow surface layer of titanium alloy penetrated by the X-rays, there is a strong variation in the level of residual stresses inside the melt track. The distribution of residual stresses is tensile within the centre of the track and compressive towards the edges. Moreover, immediately outside the melt pool the stress in the heat-affected zone is tensile. It can be expected that this will revert to compressive stress as the distance from the melt track increases. However, owing to the time consuming nature of the X-ray diffraction technique, this detail was not measured, but is confirmed by the finite element modelling (see Fig. 18).

The effect of overlapping adjacent melt tracks on the residual stress distribution is shown in Fig. 22. Overlapping melt tracks were produced by traversing the specimen by 0.70 mm between successive laser passes. This corresponds to an overlap of approximately 50 per cent of the melt top width. The sample was allowed to cool below 50 °C between each successive pass in order to eliminate any preheating effect. The data presented in Fig. 22 indicate a distribution of stresses within the first melt track (left) that is approximately similar to that plotted in Fig. 21. However, there is a progressive increase in the level of tensile residual stresses as successive adjacent melt tracks are deposited. In addition, in the case of overlapping adjacent melt tracks, which are essential to the engineering application of the laser nitriding technique, transverse cracks [i.e. perpendicular to the direction of the laser scan (Fig. 23)], as well as longitudinal cracks [i.e. parallel to the direction of the laser scan (Fig. 24)], are detected. It is reported [11] that, under a particularly broad range of processing parameters (scanning speed, power and power distribution), cracking was never detected when Ti–6Al–4V was laser melted in an inert atmosphere. However, the introduc-

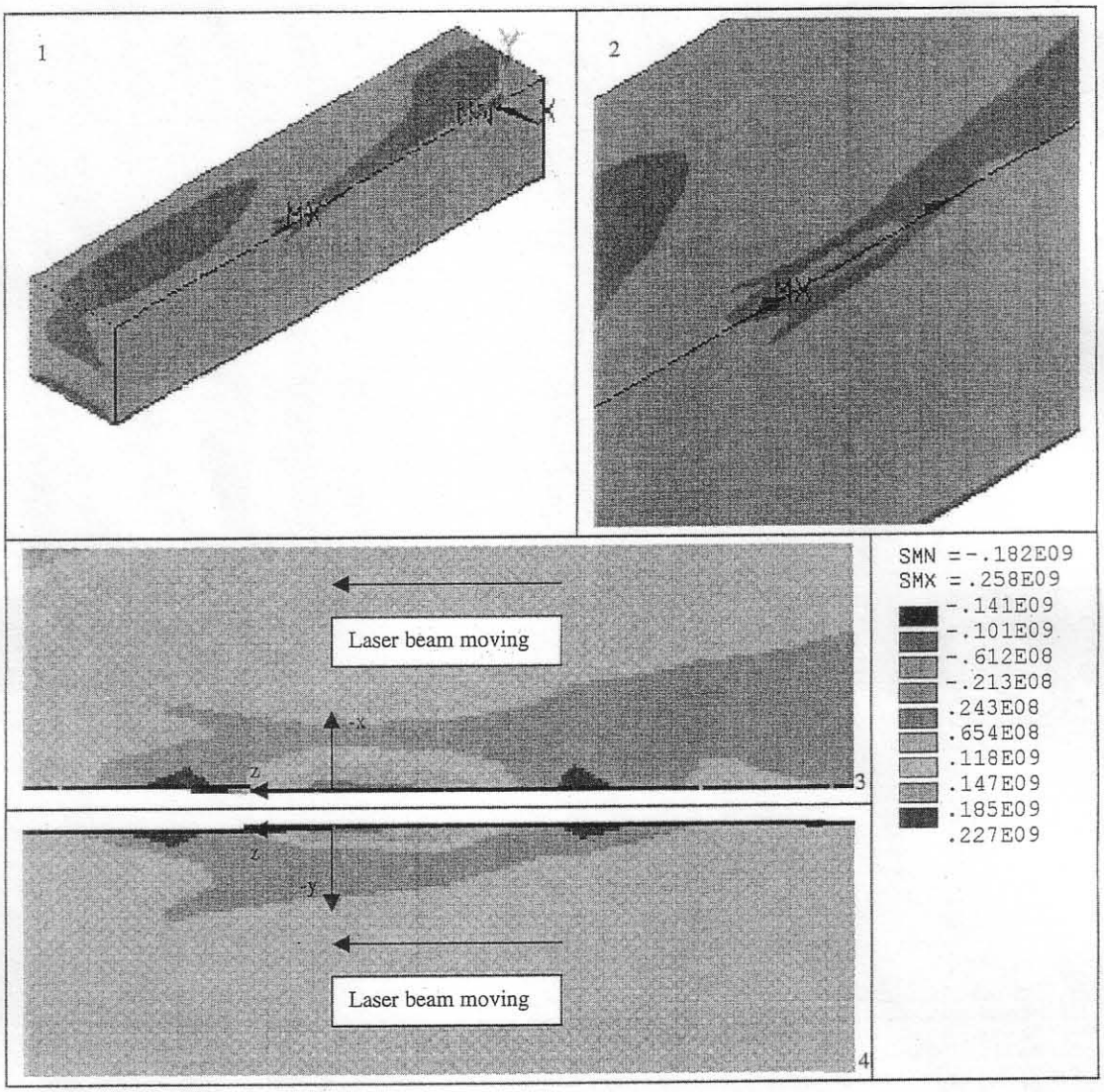

Fig. 18 Distribution of residual stresses, σ_x, during laser gas nitriding of titanium alloy Ti–6Al–4V (laser power 800 W, scanning speed 10 mm/s, shielding atmosphere 100% N_2): (1) overview; (2) top view; (3) zoom view; (4) right-hand view

tion of nitrogen into the molten pool may or may not produce detectable cracking, depending critically on the process parameters (including alloy gas dilution) [11]. A point worth stressing is that, when cracking does occur, it is in the form of transverse cracks [27]. In the present work, perhaps unsurprising are the longitudinal cracks occurring in multiple overlapping samples. This can be explained by a stepwise increase in the residual stresses with each successive, overlapping laser track up to a maximum value [28]. However, it should be noted that experiments were deliberately designed so that each overlapped track was allowed to cool below 50 °C before the following pass was carried out. This was to avoid the effect of preheating on residual stresses. However, cracking can be avoided by preheating the specimen, which will also reduce the cooling rate. The mechanism that prevents cracking by preheating increases the ductility of the titanium alloy and enhances the possibility of stress relief by plastic deformation. Figures 25 and 26 show a significant decrease in thermal gradients as well as associated cooling rates and residual stresses.

The effect of a preheating treatment to 400 °C and post-heat treatment to 600 °C for 1 h is shown in Figs 27 and 28 respectively. When preheated to 400 °C, the residual stresses are reduced to about +400 MPa. After stress relief treatment at 600 °C, the residual tensile stresses are further reduced to about +200 MPa. The effect of post-heat treatment on the phases and residual stresses of laser gas-nitrided Ti–6Al–4V samples was further investigated as a function of different nitrogen concentrations. Laser melting in an environment of 100% Ar resulted in tensile residual stresses of about

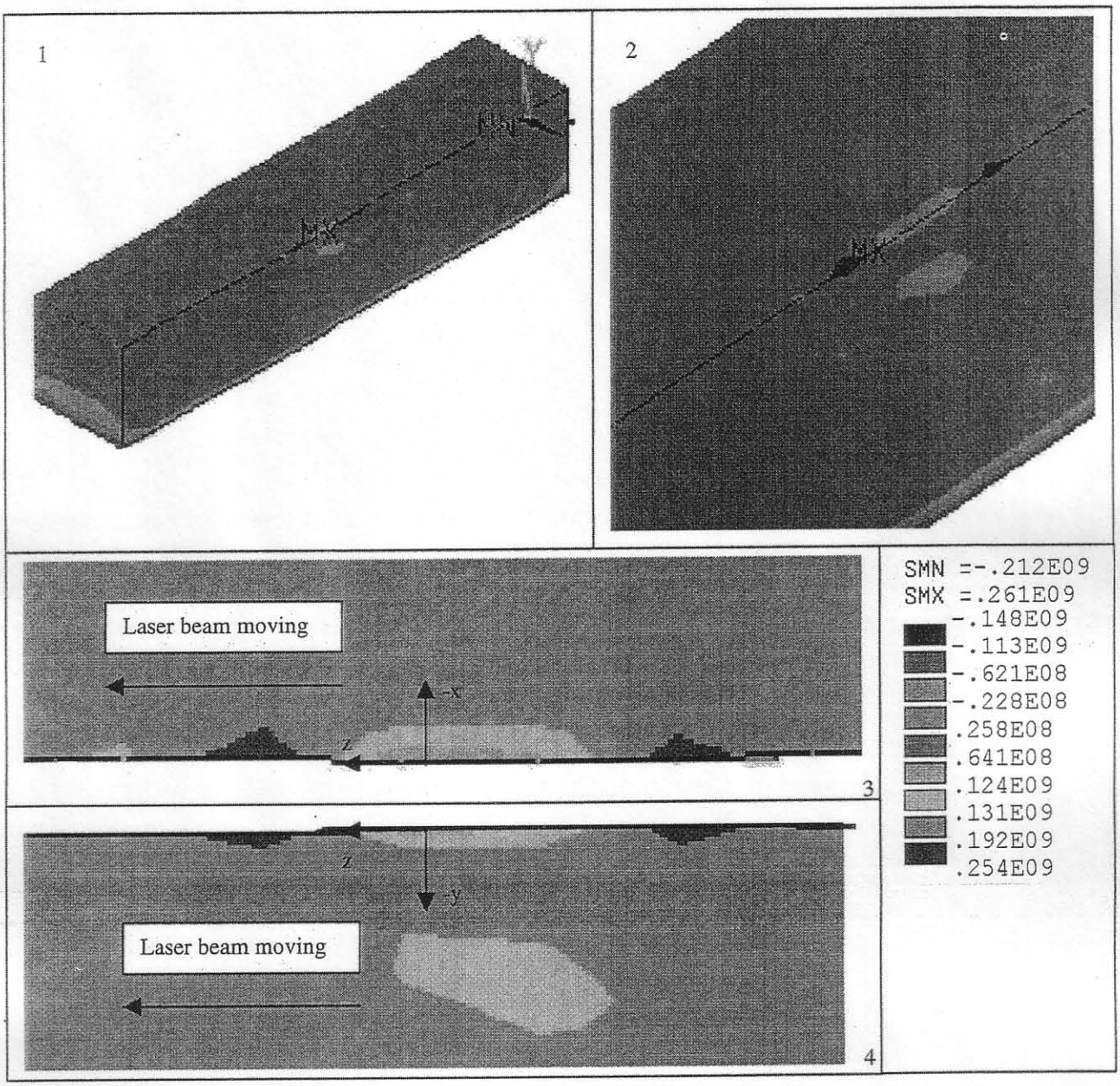

Fig. 19 Distribution of residual stress, σ_y, during laser gas nitriding of titanium alloy Ti–6Al–4V (laser power 800 W, scanning speed 10 mm/s, shielding atmosphere 100% N_2): (1) overview; (2) top view; (3) zoom view; (4) right-hand view

+400 MPa (Fig. 29). After stress relief in N_2 at 600 °C for 3 h, the residual stresses were reduced to about +50 MPa (Fig. 30). These results suggest that shrinkage in the melt zone produces residual tensile stresses and that stress relief could almost eliminate them. Phase analysis by X-ray diffraction shows that no oxides were formed either before or after the stress relief procedure (Fig. 31).

Laser surface nitriding in an environment of pure nitrogen (100 vol %) resulted in high residual stresses of about 600 MPa (see Fig. 22). However, after stress relief in N_2 at 600 °C for 3 h, the original tensile stresses became compressive (about −100 MPa) (Fig. 32). X-ray diffraction shows that titanium nitrides (TiN, $TiN_{0.9}$) are formed together with a small amount of residual Ti (see Fig. 15). The possibility of formation of $TiN_{0.9}$ instead of (or together with) TiN has been previously reported in the literature [**29**] and deserves to be discussed for a moment. Namely, according to the Ti–N equilibrium phase diagram (see Fig. 11), the titanium nitride formed at high temperatures should be TiN. However, the standard X-ray powder diffraction files for titanium

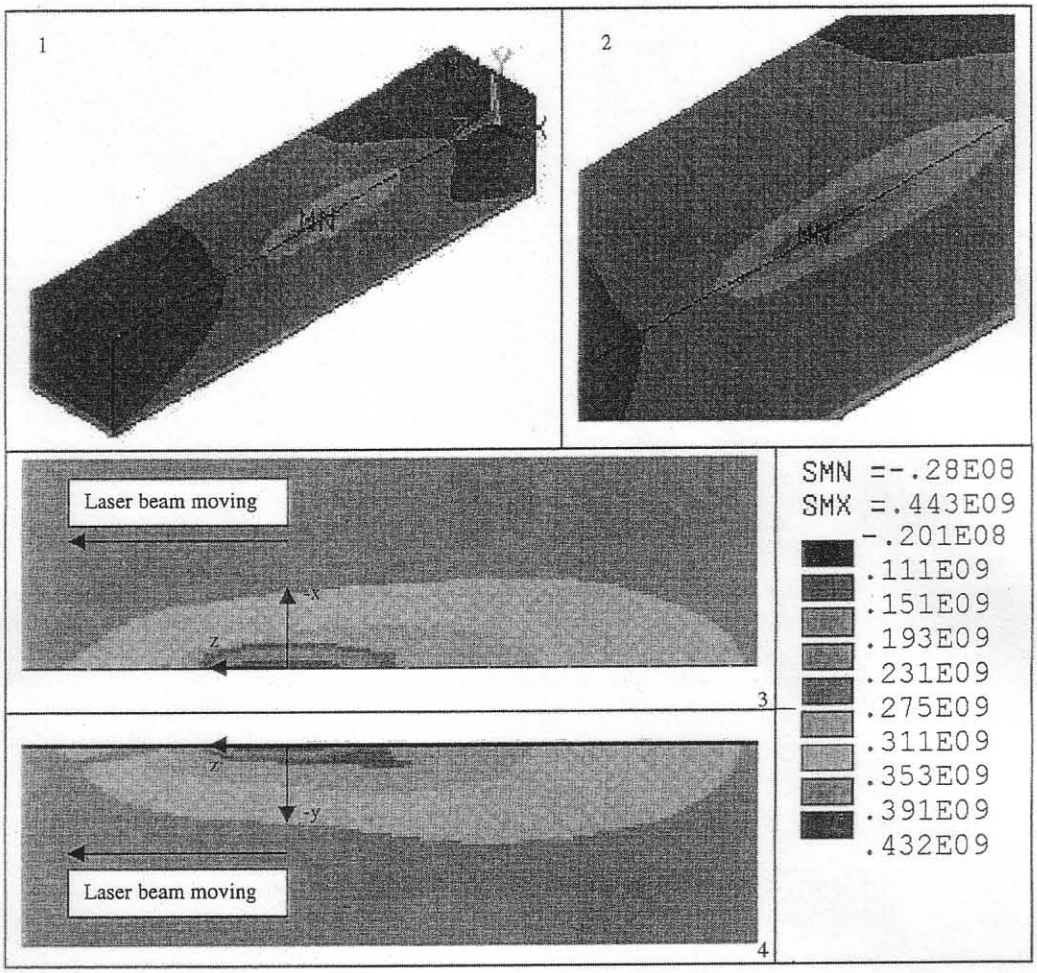

Fig. 20 Distribution of residual stresses, σ_z, during laser gas nitriding of titanium alloy Ti–6Al–4V (laser power 800 W, scanning speed 10 mm/s, shielding atmosphere 100% N_2): (1) overview; (2) top view; (3) zoom view; (4) right-hand view

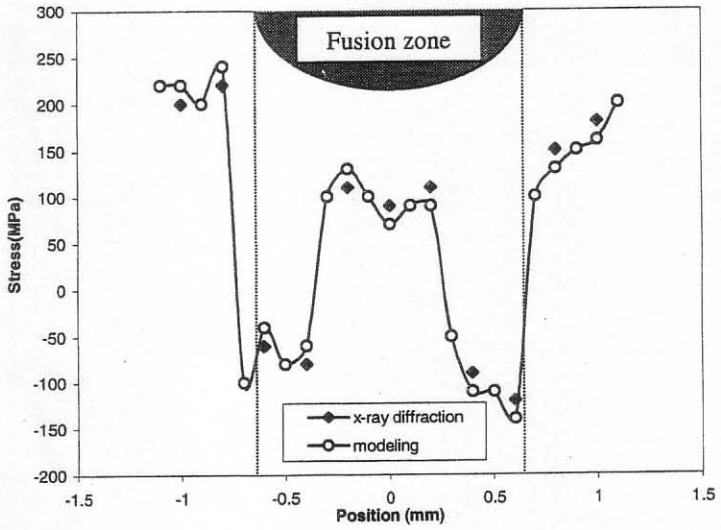

Fig. 21 Distribution of residual stresses within a single melt track on a titanium alloy Ti–6Al–4V substrate. Comparison of the results obtained by the X-ray diffraction method with those obtained by the model (laser power 800 W, scanning speed 10 mm/s, shielding atmosphere 100% N_2)

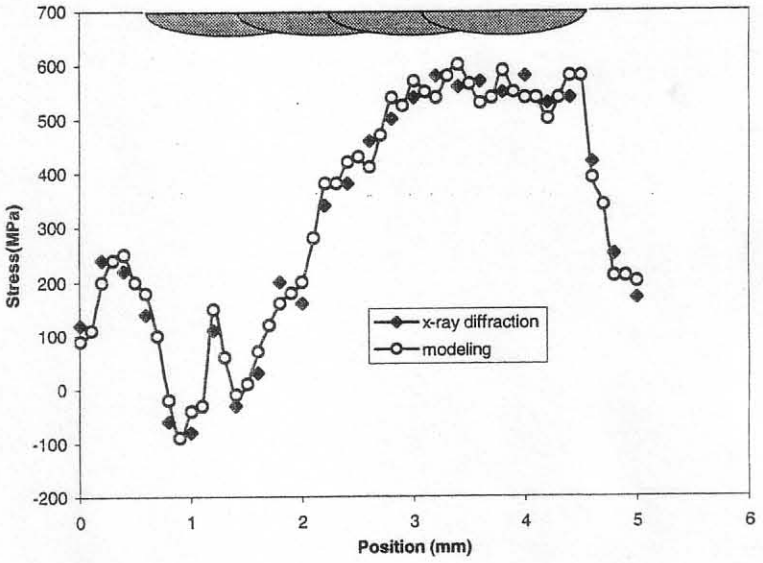

Fig. 22 Distribution of residual stresses within overlapping adjacent laser melt tracks on a titanium alloy Ti–6Al–4V substrate. Comparison of the results obtained by the X-ray diffraction method with those obtained by the model

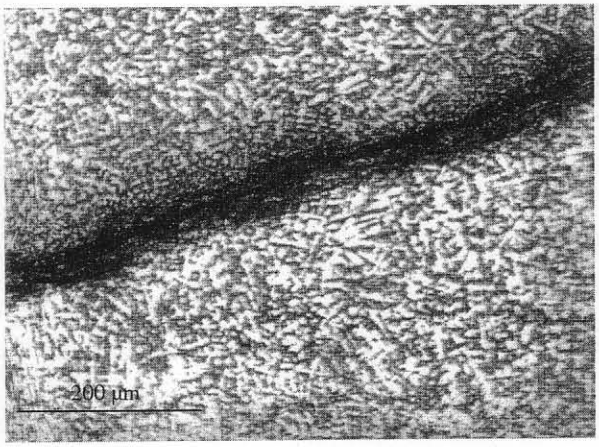

Fig. 23 Micrograph showing typical perpendicular crack formation associated with a single laser melt track

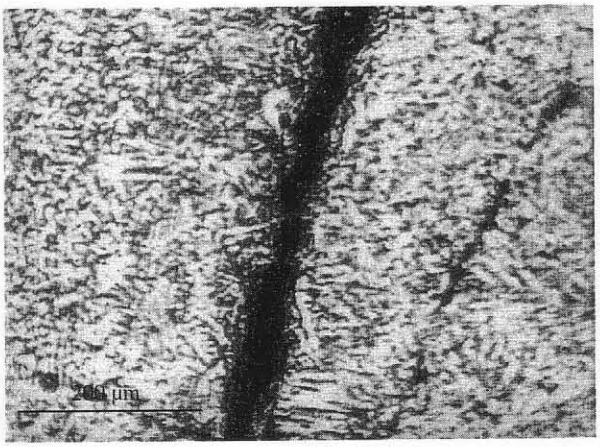

Fig. 24 Micrograph showing typical longitudinal crack formation associated with overlapping adjacent laser melt tracks

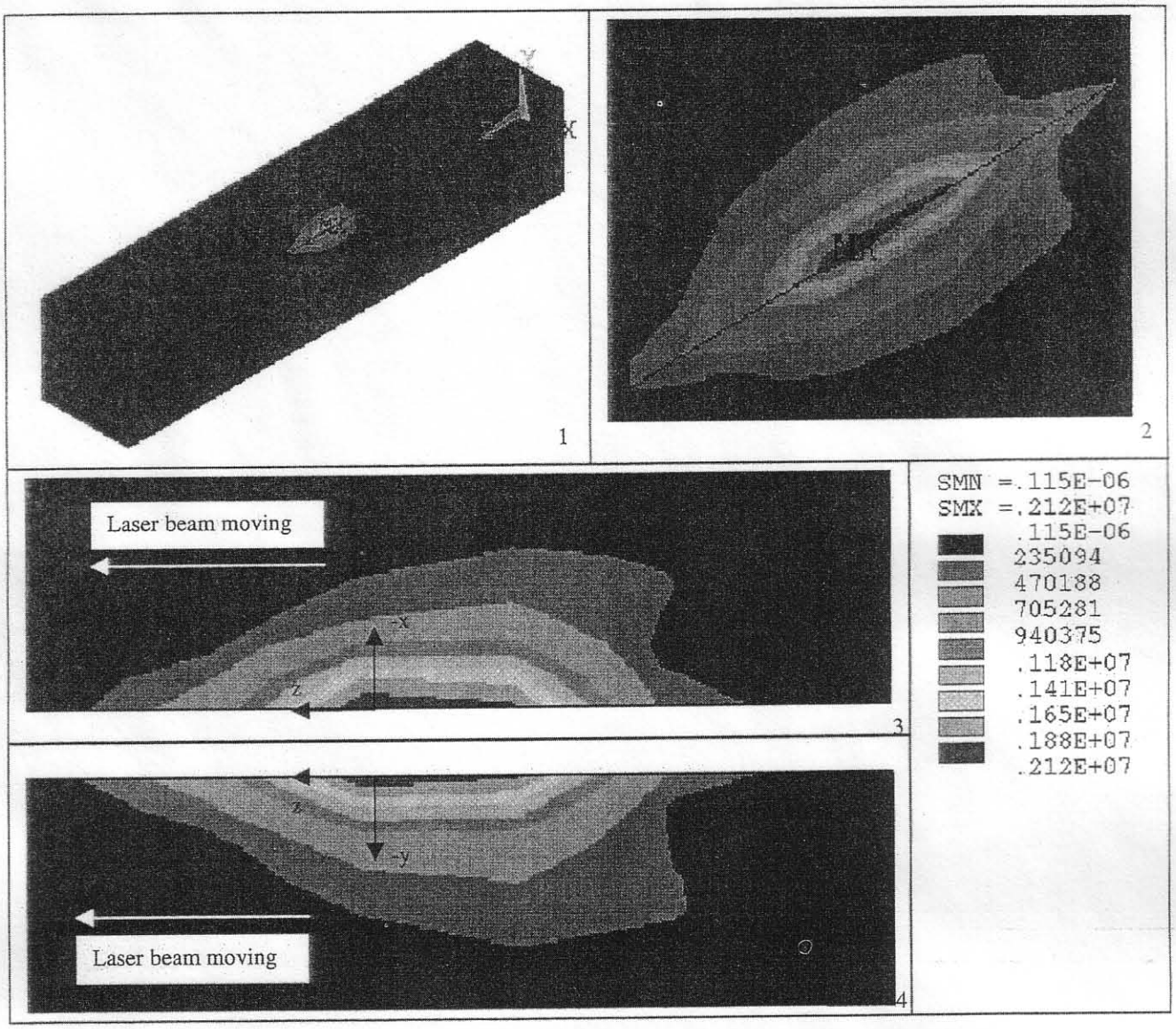

Fig. 25 Distribution of thermal gradients during the laser gas nitriding of titanium alloy Ti–6Al–4V without preheating: (1) overview; (2) zoom view; (3) top view; (4) right-hand view

nitrides show that the intensity of the TiN (111) peak is about 77 per cent of the intensity of the $TiN_{0.9}$ (200) peak, while the intensity of the $TiN_{0.9}$ (111) peak is about 4 per cent of the intensity of the $TiN_{0.9}$ (200) peak [**30**]. The measured intensity ratio between the (111) and (200) peaks in the laser-nitrided layer is about 7 per cent, which provides strong evidence for the presence of $TiN_{0.9}$ rather than TiN. This is in agreement with results reported in reference [**29**], and therefore the titanium nitride formed during laser gas nitriding may be classified as $TiN_{0.9}$. The formation of $TiN_{0.9}$ instead of TiN is attributed to the rapid solidification that is inherent to the laser nitriding process. Rapid solidification leads to a non-equilibrium state because there is not enough time available for the interaction to take place between the titanium and nitrogen to form TiN. A metastable $TiN_{0.9}$ phase is formed instead.

After stress relief, the amount of $TiN_{0.9}$ is reduced, while the amount of Ti increases. In addition, some Ti_2N peaks also appeared in the X-ray diffraction pattern (Fig. 33). According to the Ti–N equilibrium phase diagram (see Fig. 11), there is no phase transformation at 600 °C. However, as laser gas nitriding is a rapid solidification (non-equilibrium) process, the titanium nitride ($TiN_{0.9}$) is metastable, and nitrogen could also be supersaturated in the Ti phase. During stress relief, the

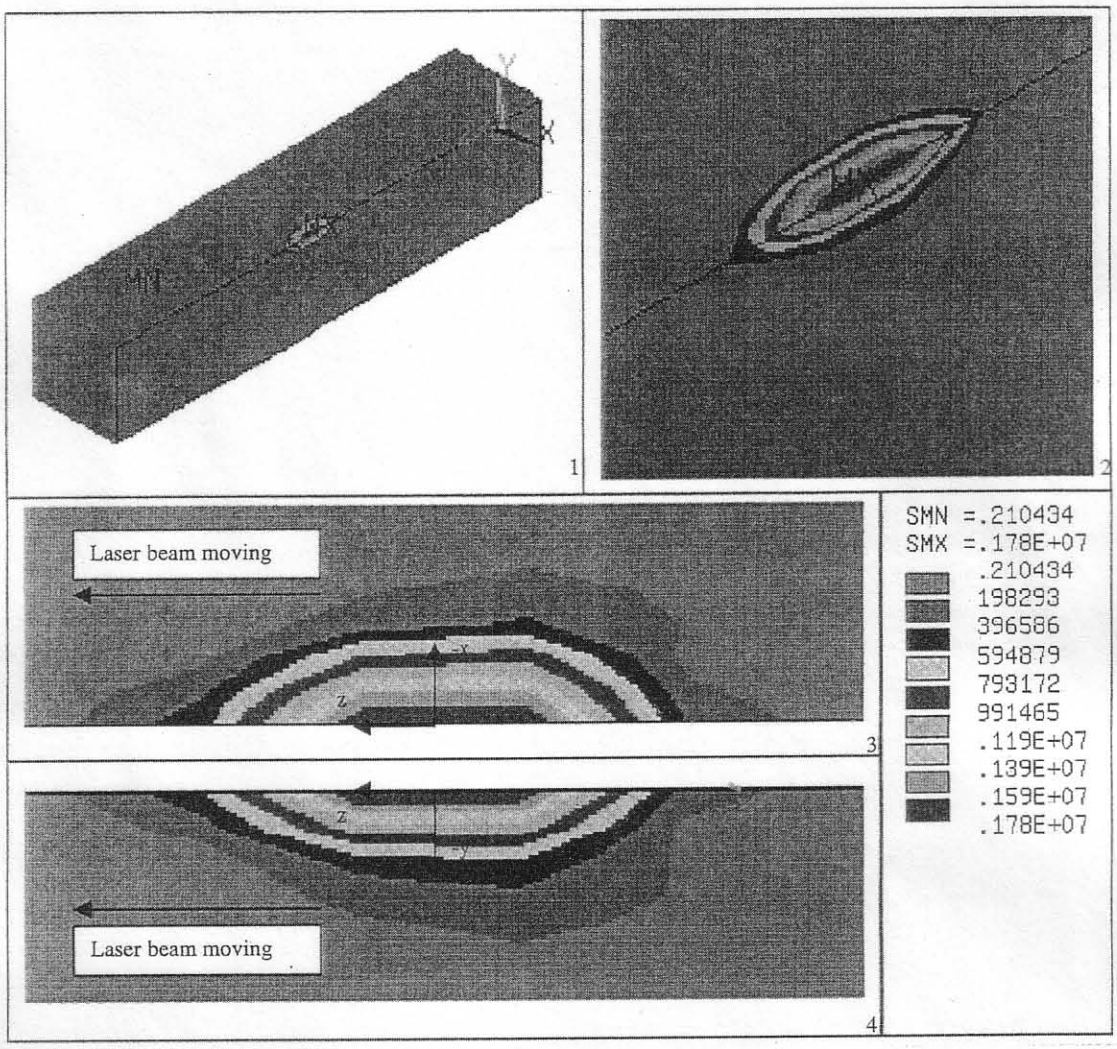

Fig. 26 Distribution of thermal gradients during the laser gas nitriding of titanium alloy Ti–6Al–4V with preheating to 400 °C: (1) overview; (2) zoom view; (3) top view; (4) right-hand view

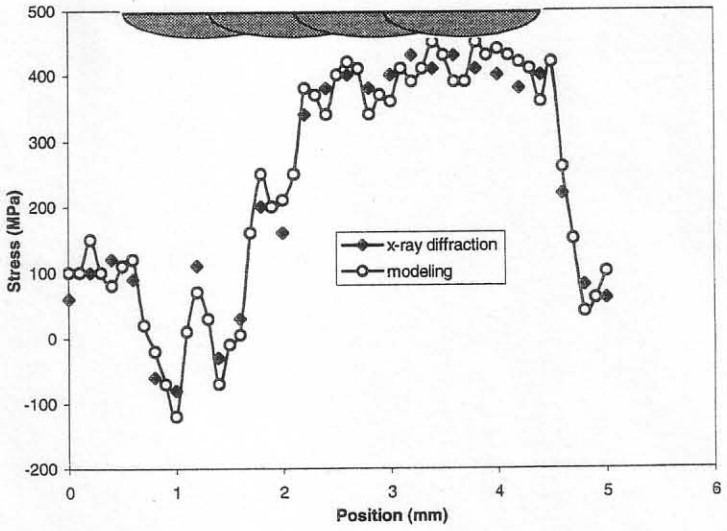

Fig. 27 Distribution of residual stresses within overlapping adjacent laser melt tracks on a titanium alloy Ti–6Al–4V substrate preheated to 400 °C. Comparison of the results obtained by the X-ray diffraction method with those obtained by the model

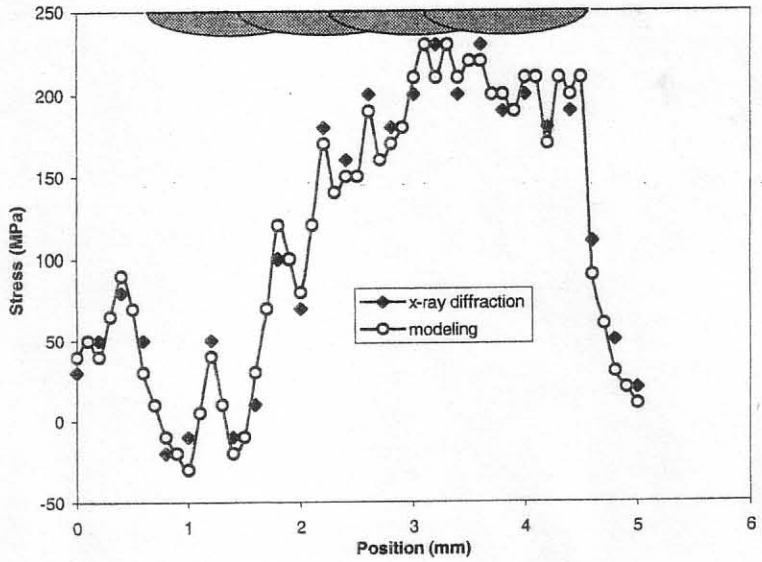

Fig. 28 Distribution of residual stresses within overlapping adjacent laser melt tracks on a titanium alloy Ti–6Al–4V substrate after post-heat treatment to 600 °C for 1 h. Comparison of the results obtained by the X-ray diffraction method with those obtained by the model

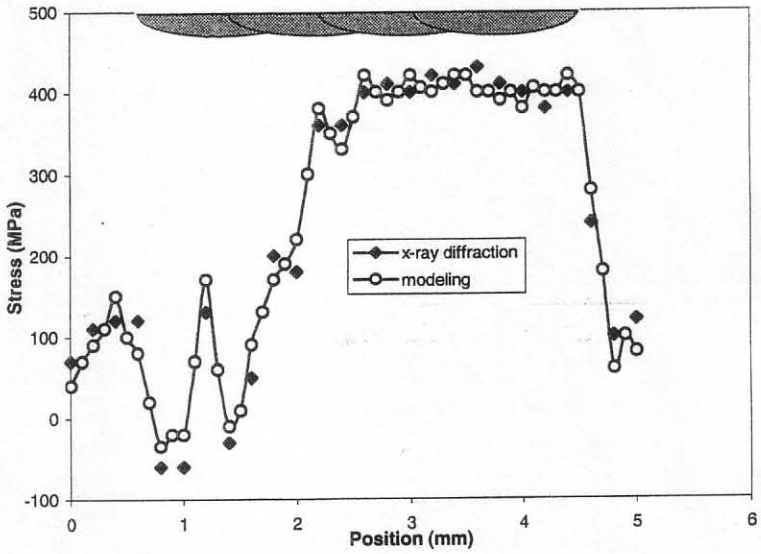

Fig. 29 Distribution of residual stresses within overlapping adjacent laser melt tracks on a titanium alloy Ti–6Al–4V substrate treated under a pure Ar (100 vol %) gas shield. Comparison of the results obtained by the X-ray diffraction method with those obtained by the model

dissolution of metastable titanium nitride and the diffusion of nitrogen from the supersaturated titanium could result in the formation of Ti_2N and an increase in the amount of Ti according to the reaction

$$x(TiN_{0.9}) \xrightarrow{600} y(Ti_2N) + zTi \quad (15)$$

This phase transformation could explain the change in the residual stress state from tension to compression since it is well understood that volume changes associated with phase transformation can result in very different stress states [**18**].

Nitriding in a diluted nitrogen atmosphere (50 vol %) produced only a small amount of titanium nitride ($TiN_{0.9}$) (see Fig. 13). This was expected since the interaction time between the melt and nitrogen in a diluted nitrogen environment decreases. The residual tensile stresses were about +500 MPa (Fig. 34). The stress relief at 600 °C for 3 h in N_2 caused the titanium nitride ($TiN_{0.9}$) to almost disappear, and some Ti_2N also

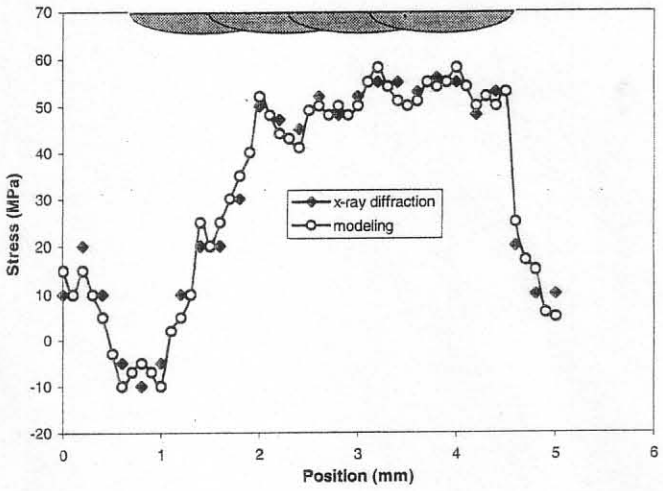

Fig. 30 Distribution of residual stresses within overlapping adjacent laser melt tracks on a titanium alloy Ti–6Al–4V substrate treated under a pure Ar (100 vol %) gas shield and after stress relief in N_2 at 600 °C for 3 h. Comparison of the results obtained by the X-ray diffraction method with those obtained by the model

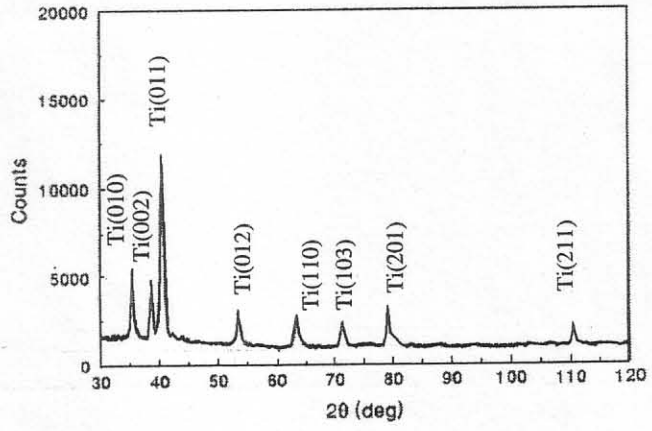

(a)

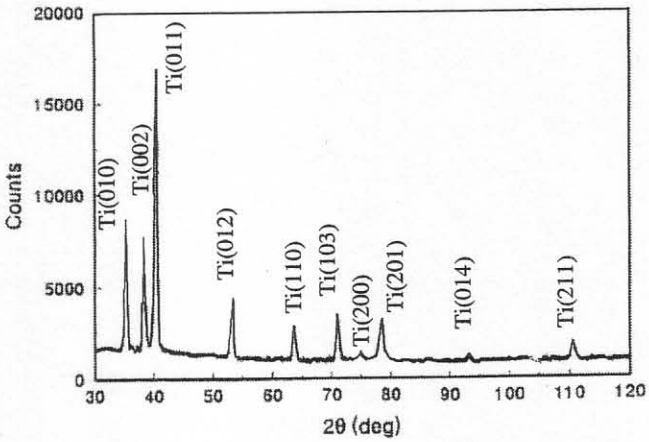

(b)

Fig. 31 X-ray diffraction spectrum taken from the titanium alloy Ti–6Al–4V surface: (a) treated under a pure Ar (100 vol %) gas shield; (b) after stress relief in N_2 at 600 °C for 3 h

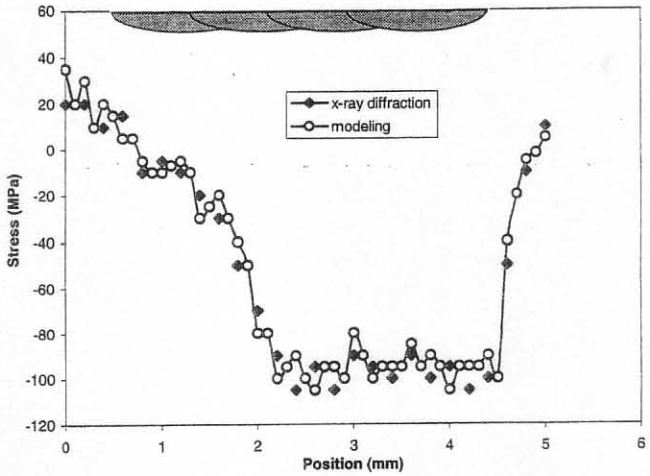

Fig. 32 Distribution of residual stresses within overlapping adjacent laser melt tracks on a titanium alloy Ti–6Al–4V substrate treated under a pure N_2 (100 vol %) gas shield and after stress relief in N_2 at 600 °C for 3 h. Comparison of the results obtained by the X-ray diffraction method with those obtained by the model

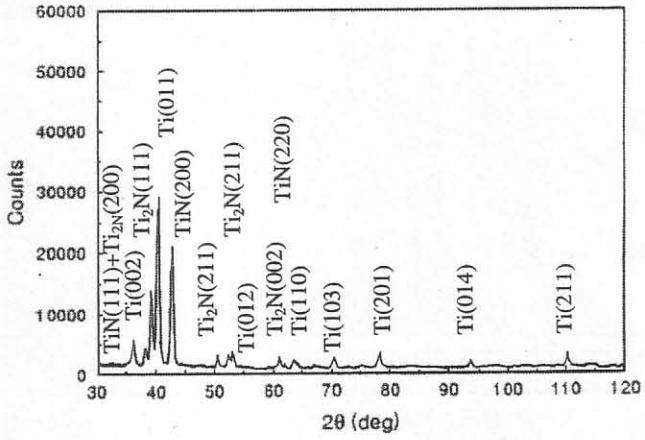

Fig. 33 X-ray diffraction spectrum taken from the titanium alloy Ti–6Al–4V surface treated under a pure N_2 (100 vol %) gas shield after stress relief in N_2 at 600 °C for 3 h

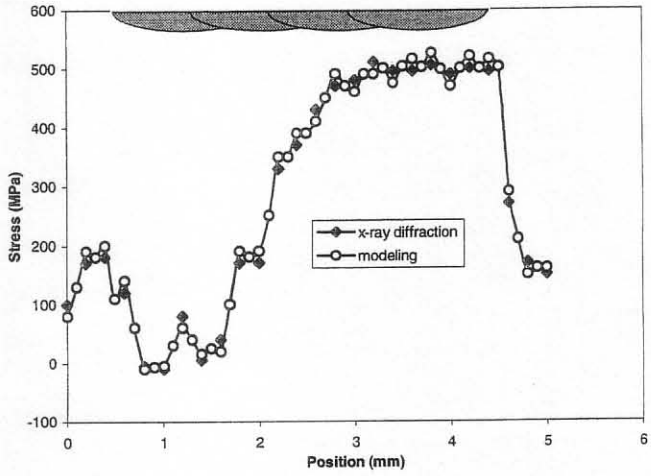

Fig. 34 Distribution of residual stresses within overlapping adjacent laser melt tracks on a titanium alloy Ti–6Al–4V substrate treated under an Ar (50 vol %)–N_2 (50 vol %) mixture. Comparison of the results obtained by the X-ray diffraction method with those obtained by the model

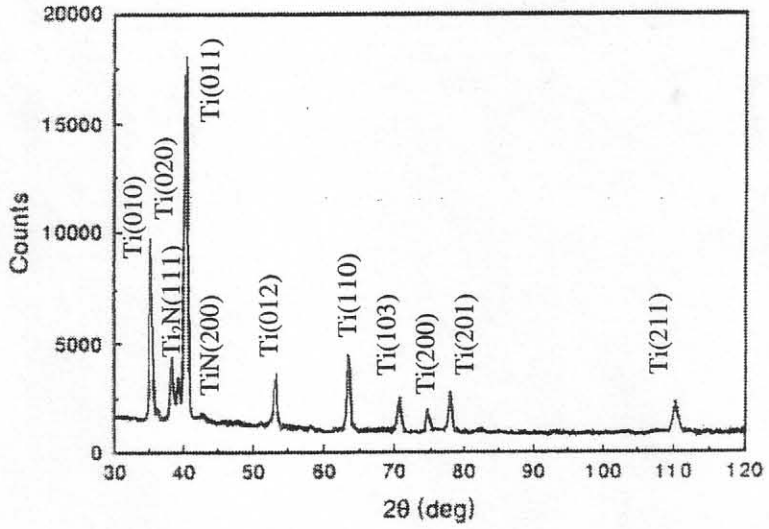

Fig. 35 X-ray diffraction spectrum taken from the titanium alloy Ti–6Al–4V surface treated under a mixture of N_2 (50 vol %) and Ar (50 vol %) after stress relief in N_2 at 600 °C for 3 h

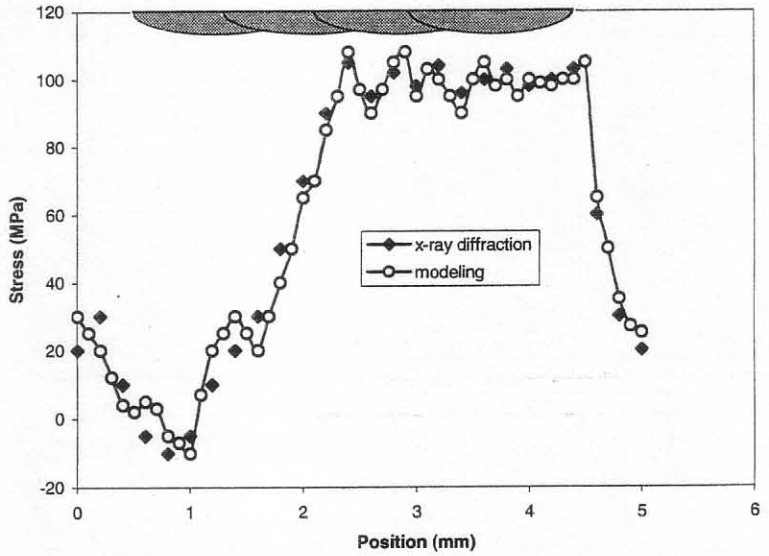

Fig. 36 Distribution of residual stresses within overlapping adjacent laser melt tracks on a titanium alloy Ti–6Al–4V substrate treated under an Ar (50 vol %)–N_2 (50 vol %) mixture and after stress relief in N_2 at 600 °C for 3 h. Comparison of the results obtained by the X-ray diffraction method with those obtained by the model

formed (Fig. 35). The residual stresses were reduced to about +100 MPa (Fig. 36).

7 CONCLUSION

A three-dimensional finite element model of the heat flow and residual stresses in laser surface nitrided Ti–6Al–4V alloy has been developed. The simulation and experimental results are in very good agreement with each other.

The simulation results provide the cross-sectional shape of the molten pool. In addition, these results are certified by the top-side image of the molten pool acquired on-line by the high-speed shutter camera. The pool is deeper at the end than at the beginning of the bead because of the heat accumulation. In reality, this means there are relations between the shape and the depth of the molten pool. Therefore, a capability of computationally predicting the FZ boundary allows the possibility of constructing a surface nitriding monitoring system based on temperature sensing and machine

vision. Furthermore, the calculated peak surface temperature can be used to correlate with a resolidified microstructure.

Modelling results of residual stress calculations are confirmed by X-ray diffraction residual stress measurements. In comparison with a single melt track, overlapping adjacent melt tracks result in an increase in the residual stresses. These data can be used to rationalize the observation that cracking may occur in a longitudinal, as well as transversal, direction. More importantly, cracking can be avoided by preheating the specimen which will decrease the thermal gradient and associated cooling rates. Cracking can also be avoided by stress relief which significantly reduces the residual tensile stress level. The main reaction that is believed to produce compressive residual stresses is

$$x(TiN_{0.9}) \xrightarrow{600} y(Ti_2N) + zTi$$

Finite element modelling of residual stresses was able to predict computationally various deviations from ideal conditions, providing information that is necessary for engineering applications.

REFERENCES

1 **Boyce, A., Morten, P. H.** and **Bell, T.** In *Metals Handbook*, 1994, Vol. 5, p. 835 (ASM International, Materials Park, Ohio).
2 **Goto, T., Tada, M.** and **Ito, Y.** *Electrochim. Acta*, 1994, **39**, 1107–1113.
3 **Elder, J. E., Thamburaj, R.** and **Patnaik, P. C.** *Surf. Engng*, 1989, **5**, 55–78.
4 **Himterman, H. E.** *Wear*, 1984, **100**, 381–397.
5 **Wilson, A., Mathews, A., Houdsen, J., Turner, R.** and **Garside, B.** *Surf. and Coatings Technol.*, 1993, **62**, 600–607.
6 **Salehi, M., Bell, T.** and **Morten, P. H.** In *Surface Modification Technologies*, 1991, pp. 991–1002 (TMS, Warrendale, Pennsylvania).
7 **Van Brussel, B. A.** and **De Hosson, J. Th. M.** *Mater. Sci. and Engng*, 1993, **A161**, 83–89.
8 **Robinson, J. M., Anderson, S., Knutsen, R. D.** and **Reed, R. C.** *Mater. Sci. and Technol.*, 1995, **11**, 611–628.
9 **Ayers, J. D., Shaefer, R. J.** and **Robey, W. P.** *J. Met.*, 1981, **33**, 19–23.
10 **Morten, P. H., Bell, T., Weisheit, A., Kroll, J., Mordike, B.** and **Sago, K.** In *Surface Modification Technologies V* (Eds T. S. Sundarshan and J. F. Braza), 1992, pp. 593–609 (The Institute of Materials, London).
11 **Mridha, S.** and **Baker, T. N.** *Mater. Sci. and Engng*, 1994, **A188**, 229–236.
12 **Khan, M. A., Madsen, N. H., Goodling, J. S.** and **Chin, B. A.** *Optical Engng*, 1986, **25**, 799–805.
13 **Giedt, W. H.** In ASME Winter Annual Meeting on *Interdisciplinary Issues in Material Processing and Manufacturing*, Boston, Massachusetts, 1987, pp. 45–57.
14 **Ule, R. L., Joshi, Y.** and **Sedy, E. B.** *Metall. Trans. B*, 1990, **21B**, 1033–1047.
15 **Rosenthal, D.** *Trans. ASME*, 1946, **68**, 849–866.
16 **Goldak, J., McDill, M., Oddy, A., House, R., Chi, X.** and **Bibby, M.** In *Advances in Welding Science and Technology*, 1986, pp. 15–20 (ASM International, Metals Park, Ohio).
17 **Wood, R. A.** and **Favor, R. J.** In *Titanium Alloys Handbook*, 1972, pp. 1–26 (Air Force Materials Laboratory, Wright-Patterson Air Force Base, Department of Defense Information Analysis Center, Ohio).
18 **Radaj, D.** In *Heat Effects of Welding; Temperature Field, Residual Stress, Distortion*, 1992, pp. 1–156 (Springer-Verlag, Berlin and New York).
19 **Makuth, D. J., Monroe, R. E., Favor, R. J.** and **Moon, D. P.** In *Titanium Base Alloys 6Al–4V*, 1967, A-18-A-19 (Defense Metals Information Center, Battelle Memorial Institute, Columbus, Ohio).
20 **Namba, Y.** In *Laser Forming in Space* (Ed. C. P. Wang), 1986, pp. 403–407 (Osaka, Japan).
21 **Li, W., Geiger, M.** and **Vollertsen, F.** *Chin. J. Lasers*, 1998, **25**(9), 859–864.
22 **Brown, S.** and **Song, H.** *J. Engng for Industry*, 1992, **114**, 441–451.
23 *ANSYS Theory Manual, Release 5.3*, June 1996 (ANSYS Inc., USA).
24 **Frewin, M. R.** and **Scott, D. A.** *Weld. J.*, 1999, **78**, 15–22.
25 **Hu, D., Labudovic, M.** and **Kovacevic, R.** In Proceedings of the 9th International Conference on *Computer Technology in Welding* (Eds T. Siewert and C. Pollock), NIST Special Publication 949, May 2000, pp. 417–424.
26 **James, M. R.** and **Cohen, J. B.** In *Experimental Methods in Materials Science*, 1958, Vol. 1, pp. 30–126 (Academic Press, New York).
27 **Mridha, S.** and **Baker, T. N.** *Mater. Sci. and Engng*, 1994, **A188**, 229–239.
28 **Kloosterman, A. B.** and **De Hosson, J. Th. M.** In International Conference on *Computer Methods and Experimental Measurements for Surface Treatment Effects*, Milan, Italy, 1995, pp. 247–254.
29 **Xue, L., Islam, M., Koul, A. K., Bibby, M.** and **Wallace, D. W.** *Adv. Perf. Mater.*, 1997, **4**, 389–408.
30 Joint Committee on Powder Diffraction Standards (JCPD), Powder Diffraction File 38-1420: TiN, and File 31-1403: $TiN_{0.9}$.